

Hyperelastic “bone”: A highly versatile, growth factor–free, osteoregenerative, scalable, and surgically friendly biomaterial

Adam E. Jakus,^{1,2} Alexandra L. Rutz,^{2,3} Sumanas W. Jordan,⁴ Abhishek Kannan,⁵ Sean M. Mitchell,⁵ Chawon Yun,⁵ Katie D. Koube,^{1,2} Sung C. Yoo,^{1,2} Herbert E. Whiteley,⁶ Claus-Peter Richter,⁷ Robert D. Galiano,⁴ Wellington K. Hsu,^{2,5} Stuart R. Stock,⁸ Erin L. Hsu,^{2,5} Ramille N. Shah^{1,2,3,9*}

Despite substantial attention given to the development of osteoregenerative biomaterials, severe deficiencies remain in current products. These limitations include an inability to adequately, rapidly, and reproducibly regenerate new bone; high costs and limited manufacturing capacity; and lack of surgical ease of handling. To address these shortcomings, we generated a new, synthetic osteoregenerative biomaterial, hyperelastic “bone” (HB). HB, which is composed of 90 weight % (wt %) hydroxyapatite and 10 wt % polycaprolactone or poly(lactico-glycolic acid), could be rapidly three-dimensionally (3D) printed (up to 275 cm³/hour) from room temperature extruded liquid inks. The resulting 3D-printed HB exhibited elastic mechanical properties (~32 to 67% strain to failure, ~4 to 11 MPa elastic modulus), was highly absorbent (50% material porosity), supported cell viability and proliferation, and induced osteogenic differentiation of bone marrow–derived human mesenchymal stem cells cultured *in vitro* over 4 weeks without any osteo-inducing factors in the medium. We evaluated HB *in vivo* in a mouse subcutaneous implant model for material biocompatibility (7 and 35 days), in a rat posterolateral spinal fusion model for new bone formation (8 weeks), and in a large, non-human primate calvarial defect case study (4 weeks). HB did not elicit a negative immune response, became vascularized, quickly integrated with surrounding tissues, and rapidly ossified and supported new bone growth without the need for added biological factors.

INTRODUCTION

The quest to discover an ideal bone graft material that is compatible with the extensive variety of osseous tissue–related medical indications has been an ongoing challenge. Although there are numerous clinical products used today as bone void fillers or temporary scaffolds (1) and an extensive body of literature that reports potential new bone-related biomaterials, these products and their surgical implementation suffer from substantial technical, surgical, and manufacturing/scaling shortcomings (2–4). First, an ideal bone graft material is safe and efficacious *in vivo* (that is, it should not elicit a strong immunoinflammatory host response or cause other undesirable biological responses while repairing and regenerating damaged or missing bone). Second, the material must be rapidly and easily deployed in the operating room by surgical teams (5). Last, to be translatable, it must be able to be produced at the relevant scales (construct size and number) and widely available at comparable or lower cost than existing clinical products, although this may be difficult to define and quantify at the research stages (5). Many bone-grafting products on the market and reported in the literature, often composed of calcium phosphates (CaP), polyesters, or composites of the two, excel at one or two of these criteria, but none excel at all three.

Synthetic and naturally derived CaP-based ceramics have been commonly used to treat bone defects due to their inherent bioactivity (2, 6, 7). However, the same stiff mechanical characteristics of ceramics that are partially responsible for this osteogenic bioactivity make their surgical implementation challenging or inefficient. For example, porous ceramic constructs cannot be easily shaped and resized by surgeons on demand to better accommodate the defect site (8). Additionally, ceramic constructs are not amenable to minimally invasive surgical methods because they cannot be deformed without failing through fracture. Therefore, CaP-based products have different formulations—such as granules, malleable putties, or injectable cements created with plasticizers, monomers, and water—so that they can be packed into the surgical sites (9, 10). Nevertheless, these approaches suffer from deficiencies. Packed granules or putties, as well as injected bone cements, are often washed away because of intraoperative bleeding within the defect site (10). Putties that harden upon placement often transfer significant heat as a result of the chemical curing process (11) and can damage surrounding tissues. The most important is the fact that CaP granules and putties have minimal interconnected porosity (10, 12), which hinders host-implant integration, vascularization (12), and patient recovery while also increasing susceptibility to inflammation, infection, and revision surgeries.

Over the past two decades, much effort has been applied toward creating porous bioceramic and bioceramic composite constructs—from the traditional freeze-casting and gas-foaming methods that result in heterogeneously porous foams (13–20) to the emerging wide variety of additive manufacturing (AM) and three-dimensional (3D) printing technologies that can be used to create ordered porosity and user-defined constructs. These newer technologies have been used to make an array of CaP-based porous materials and structures, including some that are made of synthetic hydroxyapatite (HA), a highly bioactive ceramic (21, 22).

¹Department of Materials Science and Engineering, Northwestern University, Evanston, IL 60208, USA. ²Simpson Querrey Institute for BioNanotechnology, Northwestern University, Chicago, IL 60611, USA. ³Department of Biomedical Engineering, Northwestern University, Evanston, IL 60208, USA. ⁴Department of Surgery, Division of Plastic and Reconstructive Surgery, Northwestern University, Chicago, IL 60611, USA. ⁵Department of Orthopaedic Surgery, Northwestern University, Chicago, IL 60611, USA. ⁶Department of Veterinary Pathobiology, University of Illinois, Urbana, IL 61822, USA. ⁷Department of Otolaryngology—Head and Neck Surgery, Northwestern University, Chicago, IL 60611, USA. ⁸Department of Cell and Molecular Biology, Northwestern University, Chicago, IL 60611, USA. ⁹Department of Surgery, Division of Organ Transplantation, Northwestern University, Chicago, IL 60611, USA.

*Corresponding author. Email: ramille-shah@northwestern.edu

These have been fabricated with established ceramic AM methods (23), such as particulate slurry extrusion or powder bed-based inkjet binding followed by sintering (24–27), which require additional high-temperature processing steps and result in brittle final products unfriendly to surgical applications. This high-temperature processing is also incompatible with the direct incorporation of agents such as antibiotics (28, 29), growth factors, and other advanced organic-based therapeutics (30), directly into the material, which can be used to enhance and hasten tissue integration and regeneration (31).

It is for these reasons that the field has focused on CaP-polymer composites, including those produced via room temperature or hot-melt extrusion-based 3D printing (32–34) or other forms of AM (35, 36). Nevertheless, these composites often still have suboptimal material, handling, and/or biological properties: Although composites with CaP, whether in hydrogel (37) or 3D-printed form (32–34), often have improved stiffness (elastic and compressive moduli) over pure polymers and increased mechanical elasticity or malleability over pure CaPs (5), the polymeric component often physically encapsulates the bioactive CaP particles, isolating them from the tissue and mitigating their therapeutic potential. In addition, many 3D-printed composites are fabricated with hot-melt fused deposition modeling or laser sintering techniques, which require temperatures greater than 100°C. This high-temperature processing precludes direct incorporation of biological molecules or factors (33) and is too slow for mass fabrication, with linear deposition rates not greater than 5 mm/s or volume deposition rates not greater than 1 mm³/s. Although these composites often do not undergo brittle fracture, their bioactivity is often limited, requiring surface modification with costly biomolecules or other factors (38–40), which also complicate regulatory approval and translatability. Here, we report a new synthetic osteoregenerative biomaterial, which we have called hyperelastic “bone” (HB), that avoids the technical, surgical, and manufacturing limitations of current bone graft materials.

RESULTS

Examples of HB ink design, 3D printability, and versatility

We synthesized HB particle-laden liquid 3D inks by combining ceramic powder (HA) and polycaprolactone (PCL) or poly(lactic-co-glycolic acid) (PLGA) (9:1 by weight) to produce hydroxyapatite-polycaprolactone (HAPCL) or hydroxyapatite-poly(lactic-co-glycolic acid) (HAPLGA), respectively, in a trisolvant mixture comprising excess dichloromethane (DCM; evaporant), 2-butoxyethanol (2-Bu; surfactant), and dibutyl phthalate (DBP; plasticizer). We recently illustrated that these new 3D ink systems containing biomedical elastomers can be used to rapidly 3D-print graphene inks into highly electrically conductive structures comprising many layers that exhibit strong neurogenic properties and excellent handling characteristics (41). We have also recently adapted this process to create 3D printable metal oxide (ceramic) and metallic inks, which could be thermally processed into an extensive variety of metals and alloys (42). We selected PLGA and PCL as the binders for HB inks because of their extensive use in medicine and tissue engineering (43–46). With these particular elastomers, we 3D-printed solid HB structures comprising many hundreds of layers (movie S1) from liquid inks (Fig. 1A, inset). The resulting structures did not require further postprinting processing (other than rinsing and sterilization) before use and exhibited mechanical and physical properties that permitted further manipulation. For example, a 3D-printed HAPLGA sheet could be rolled, folded, and cut (Fig. 1A and

movie S2) to create architectures that might otherwise not be possible to 3D-print directly because of the large, unsupported overhangs. An example of how HB could be used surgically is illustrated in Fig. 1C, where HB cylinders of various sizes were 3D-printed (inset) and the correct size was selected. They were snugly slipped onto the terminal regions of soft tissue human tendon allograft, cut to size, and sutured to the graft. An augmented graft such as this could be used in arthroscopic procedures for replacing damaged anterior cruciate ligaments (ACLs), where it may accelerate and strengthen ligament-to-bone healing within bone tunnels after ACL reconstruction (47).

We also rapidly 3D-printed HB inks into anatomically scaled, patient-specific grafts, such as an adult human mandible (Fig. 1B). We achieved linear print speeds as high as 15 cm/s (the hardware limits of the instrument), with no drying time required before handling the completed object. This linear deposition rate equates to volume deposition rates as high as 275 cm³/hour, from a single nozzle, or total object(s) volume of 550 cm³/hour when the architecture was 50% porous. We were able to 3D-print, wash, sterilize, and prepare for use this mandible in less than 3 hours. We custom-made HB into complex scaffold designs such as porous long-bone sleeves, which could both stabilize a long-bone fracture and promote regeneration across the defect length (fig. S1A). Additionally, unlike many other 3D printable material systems, HB inks could be used as self-adhesives, allowing independently 3D-printed objects made of the same or similar materials to be seamlessly fused together. Individually 3D-printed components were merged to form highly complex geometries, which would be impossible to 3D-print as one monolithic object (Fig. 1D). Furthermore, we used HB inks as flexible coatings on other implantable materials, such as metallic screws (fig. S1B); this application is similar to adding bioceramic coatings to these screws, a process shown to improve tissue integration (31). Last, the ability to synthesize and 3D-print HB inks under ambient conditions with no need for further sintering or chemical cementation allowed incorporation of biological factors and molecules, such as proteins (Fig. 1E), peptides, genes, and antibiotics (fig. S1C) (48, 49), which may enhance tissue regeneration and reduce infection.

HB microstructure

To better understand the unique characteristics of HB, we compared fibers created with different ink formulations and printing methods (hot-melt extrusion versus solvent-based room temperature extrusion) (Table 1). We examined the microstructures of (i) HA/PCL (1:1 by weight) hot-melt-extruded fiber; (ii) HA/PCL (1:1 by weight) room temperature, trisolvant-based printed fiber; (iii) HA/PCL (9:1 by weight) room temperature printed fiber using only DCM as the solvent; and (iv) HA/PCL (9:1 by weight) room temperature, trisolvant-based printed fiber (HAPCL) (Fig. 2, A to D). Hot-melt fibers, which have been used in tissue engineering research (32, 50), are characterized by slow extrusion rates (0.5 to 5 mm/s) and dense polymer matrices encompassing the HA particles (Fig. 2A and fig. S2). This is in contrast to the solvent-based, room temperature 3D-printed fiber microstructures, which are rough and have a nano- and microporous architecture (Fig. 2, B to D). Furthermore, there are differences in the elastomer matrix morphology: The elastomer in the trisolvant-based printed fibers forms a smooth continuous matrix joining the particles (Fig. 2, D and G), whereas the single-solvent fibers are characterized by a fine web-like network of elastomer joining adjacent HA particles (Fig. 2, C and F).

We hypothesize that the microstructural differences between the single- and trisolvant fibers are a result of the interplay between solvent evaporation and polymer condensation. In both cases, inks begin as

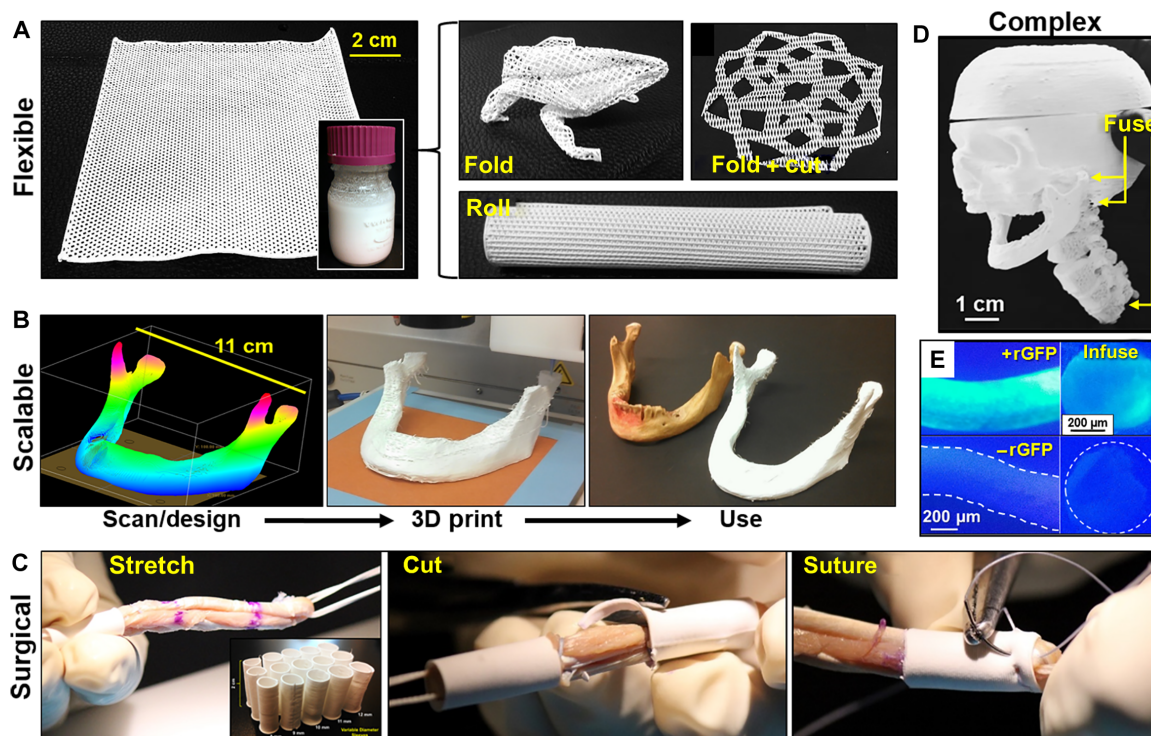


Fig. 1. Versatility, scalability, and manipulation of 3D-printed HB. (A) Easy to synthesize volumes (~100 ml shown) of liquid-based HB inks (inset) can be 3D-printed into a variety of structures: 3D-printed 12 × 12-cm HAPLGA sheet comprising three layers, which can be manipulated in a variety of ways, including rolling, folding, and cutting. Origami methods may be used to create complex folded structures, whereas kirigami methods can produce complex structures from strategic folding and cutting. (B) Full-scale, anatomically correct parts, such as a human mandible, comprising >250 layers, can be designed, 3D-printed from HAPLGA, and washed to rapidly produce a ready-to-implant object. Final image shows 3D-printed mandible

next to an adult cadaveric human mandible. (C) Photograph series illustrating that custom-sized HAPLGA sleeves can be snugly stretched around, cut, and sutured to a soft tissue, such as human cadaveric tendon, facilitating arthroscopic ACL repair and replacement surgery. (D) Independently 3D-printed HAPLGA miniature-scale versions of a human skull, skull cap, mandible, and upper thoracic seamlessly fused together to create highly complex structures by using HB ink applied to points of contact. (E) Black light-illuminated optical photographs of the outside and internal cross sections of HAPLGA fiber with (top) and without (bottom) incorporated recombinant green fluorescent protein (rGFP).

Table 1. Summary of formulations, material preparation, 3D printing process, and additional characteristics of the HA-polymer composite systems discussed throughout this work. The two materials, HAPCL and HAPLGA, are collectively referred to as HB. 3DP, 3D printing.

	Solid composition (%)	Solvent composition (%)*	3DP preparation	3DP conditions	3DP rates (mm/s)	Solidification mechanism	Mechanical characteristics
Trisolvent (HAPCL) (9:1)	HA: 90 PLGA: 0 PCL: 10	DCM: 50 2-Bu: 33 DBP: 17	Ambient wet mixing	Ambient	0.5–150 [†]	DCM evaporation	Elastic
Trisolvent (HAPLGA) (9:1)	HA: 90 PLGA: 10 PCL: 0	DCM: 50 2-Bu: 33 DBP: 17	Ambient wet mixing	Ambient	0.5–150 [†]	DCM evaporation	Elastic
Hot-melt (1:1)	HA: 50 PLGA: 50 PCL: 0	DCM: 0 2-Bu: 0 DBP: 0	Dry mixing and melting at 200°C	200°C	0.1–5	Temperature-induced	Brittle
Trisolvent (1:1)	HA: 50 PLGA: 0 PCL: 50	DCM: 50 2-Bu: 33 DBP: 17	Ambient wet mixing	Ambient	0.5–20	DCM evaporation	Plastic
Single-solvent (9:1)	HA: 90 PLGA: 0 PCL: 10	DCM: 100 2-Bu: 0 DBP: 0	Ambient wet mixing	Ambient	>50	DCM evaporation	Brittle

*Estimation based on initial volume of solvents used for ink synthesis and volume change after sufficient evaporation of DCM. [†]Hardware speed limitations of the 3D printing platform used in this work. Higher speeds may be possible with other hardware.

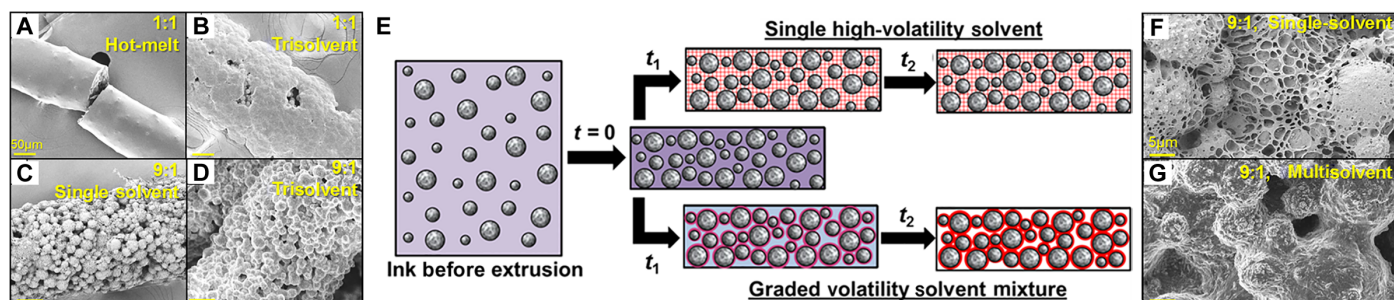


Fig. 2. Microstructural characteristics of HB and related 3D-printed systems. (A to D) Scanning electron microscopy (SEM) micrographs of representative fibers produced by HA/PCL (1:1 by mass) hot-melt (A), HA/PCL (1:1) room temperature solvent mixture (B), HA/PCL (9:1) room temperature with DCM only (C), and HA/PCL (9:1) with a trisolvent (HAPCL) (D). (E) Schematic

representation of proposed HA and elastomer distribution within fibers with single- or graded-solvent mixtures, as a function of time after extrusion. Higher-magnification SEM micrographs of DCM solvent only (F) and HAPCL microstructures (G). Details regarding material compositions and preparations can be found in Table 1.

particles homogeneously dispersed within elastomer-rich solutions (Fig. 2E). Immediately upon extrusion ($t = 0$), local particle density increases as a result of shearing forces (51). Once exposed to air, most of the DCM rapidly evaporates (t_1). In the single-solvent system, composed only of DCM, this results in rapid precipitation of all dissolved elastomer homogeneously throughout the fiber volume, resulting in a crater-web microstructure (Fig. 2F), which is characteristic of extreme “solvent popping” commonly observed in paints and other coatings when the suspending solvent evaporates too quickly. This leaves solid surface films that trap remaining solvent beneath, which eventually vaporizes and forcefully emerges through the solidified surface in the form of popping bubbles. The resulting thin elastomeric webbing presents concentrated regions of high stress and results in brittle structures that are unable to absorb significant loads without failing. In the trisolvent system, however, the two additional low-volatility solvents slow elastomer precipitation, permitting it to preferentially coat particles (t_1). Enough elastomer precipitates onto the particles to form robust interparticle bridges, whereas the inability for the spherical HA particles to densely pack results in interparticle pores (Fig. 2G). Over the course of several minutes (t_2), the remaining minority solvents evaporate, slowly precipitating the last of the solubilized material onto previously precipitated elastomer (52). The retention of the two minor solvents after initial DCM evaporation also immediately enables adjacent fibers and layers to fuse during 3D printing. This likely mitigates interlayer delamination and results in monolithic objects that can be handled immediately after being 3D-printed.

HB mechanical properties. Although not as elastic as their pure polymer counterparts (fig. S3B), both HAPLGA and HAPCL retain a high degree of elasticity, capable of undergoing $36.1 \pm 4.3\%$ and $61.2 \pm 6.4\%$ strain and having similar tensile elastic moduli of 4.3 ± 0.4 MPa and 10.3 ± 1.3 MPa, respectively. Hot-melt-extruded and DCM-only solvent-based materials were too brittle to be accurately tested under tension. Additionally, DCM-only solvent-based inks were exceptionally difficult to 3D-print into high-fidelity multilayered structures because the extruded fibers dried too quickly and did not adhere well to previously deposited material, making multilayer 3D printing particularly difficult.

The microstructural characteristics of HB permitted fibers to undergo various modes of deformation while being able to recover almost completely upon unloading (Fig. 3A and fig. S4). In all instances, macroscopic deformation resulted from the elastomer matrix straining under loads, pulling and pushing embedded particles along with it. Porosity within the

fibers enabled rigid particles to translate while limiting direct, incompressible interactions with each other. Upon compressive loading, excess pore space was eliminated as particles flowed with the straining elastomer to fill the open volume. Tensile loads were carried almost entirely by the elastomer, and under extreme strains, temporary separation between the elastomer and particle surfaces occurred (fig. S4E). However, because the HA particles were physically encapsulated within the elastomer and not covalently bound to it, these interfacial tensile voids were not permanent and disappeared upon unloading. The elastomer produced antiparallel restoring forces upon unloading, which manifested itself as a macroscopically observable elastic response (large, recoverable deformation), with the HB returning to near-net shape over many cycles (fig. S4, D and G). For porous HB constructs that were 3D-printed into defined architectures, the previously defined compression, tension, and bending deformation modes were combined to impart elastic properties throughout the entire construct. Although the geometry and porosity of the 3D-printed object affected the ultimate mechanical behavior, simple 90° cylinders (printed fibers oriented perpendicular to adjacent layers) could be cyclically compressed up to 40% strain and rapidly returned to near-original form immediately after each cycle (Fig. 3A), with full recovery occurring over the course of minutes (fig. S4H). This behavior was not limited to quasi-static loading but is also evident under dynamic loading, such as a hammer impact; 3D-printed HB constructs, despite being composed of 90 weight % (wt %) ceramic, did not shatter, catastrophically fail, or permanently deform under high-impact loads (unlike hot-melt printed samples) but, rather, rebounded to their original form (movie S3).

Although there are numerous bone-grafting indications that would not require HB to be under direct and substantial mechanical loads, such as those related to the craniofacial, torso, upper spinal, and upper extremity regions, it is nonetheless important to investigate the loading limits of HB in an anatomically scaled scenario, such as those experienced in the adult femur. To do so, we 3D-printed a 4-cm-long (135 layers) section of an anatomically correct HB midfemoral construct from a digital file (Fig. 3B) with a 600- μm nozzle. The construct was given a hollow shaft and $\sim 25\%$ porous cortex (Fig. 3, C and D), emulating the natural interior and cortical regions of natural femoral bone, and mechanically compressed in both the axial and longitudinal directions. Under uniaxial longitudinal loading, the femoral HB construct was capable of supporting about 650 N (~ 150 pounds) before the onset of plastic deformation at 10% strain (Fig. 3E, 2), at which point the construct begins

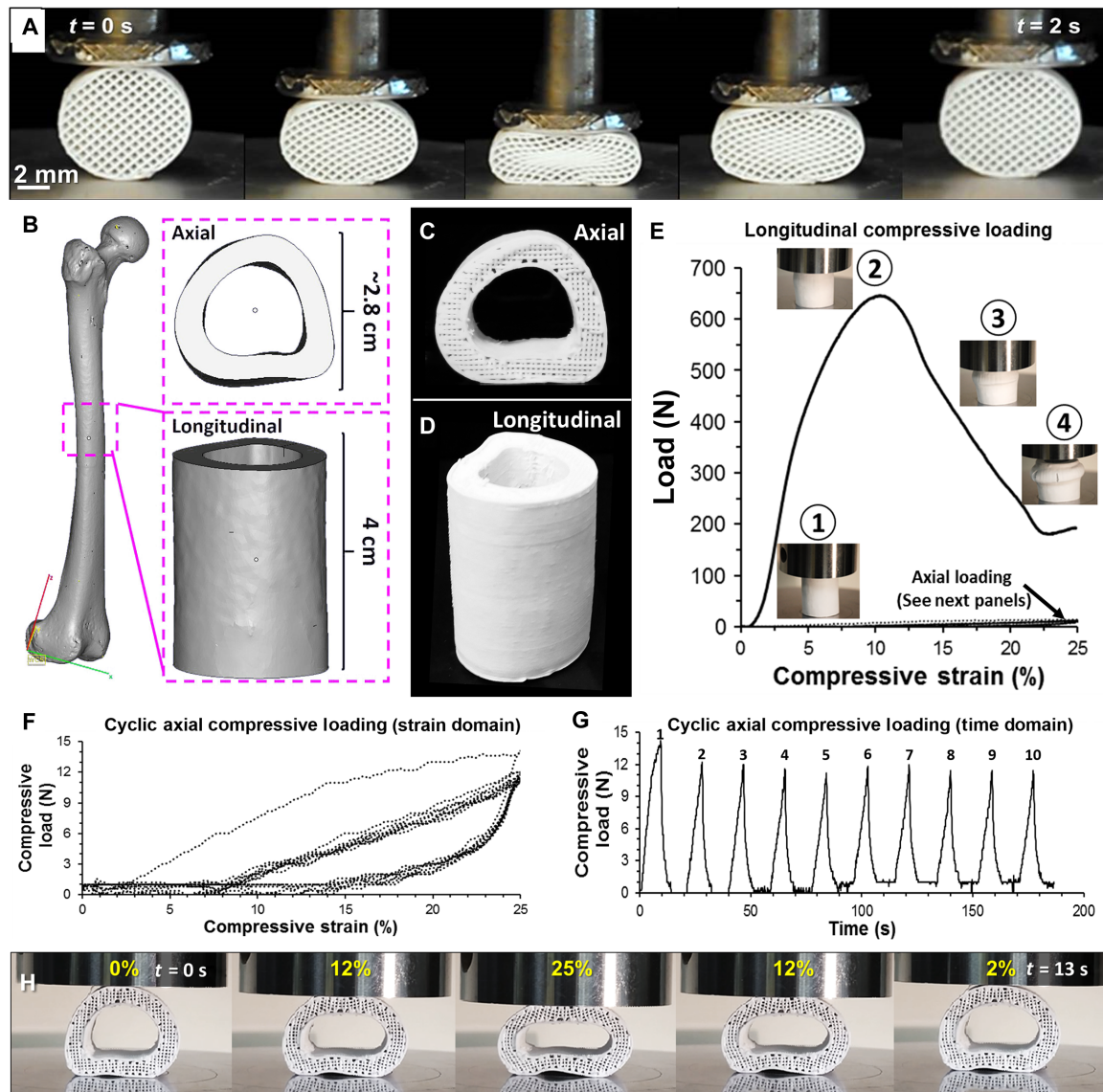


Fig. 3. HB mechanical properties. (A) Photograph series showing the compression and recovery of a 1-cm-diameter 3D-printed HAP/LGA cylinder over a single compression cycle. (B) Digital representation of average adult human femur and corresponding femoral midshaft section longitudinal and axial views. Axial (C) and longitudinal (D) views of 3D-printed HB femoral midshaft construct using digital file shown in (B). (E) Longitudinal compressive loading profile of HB femoral midshaft (D) and corresponding photo-

graphs at indicated percent strain points. Plastic deformation of HB femoral midshaft begins at 2 (10.3% strain) and proceeds to buckle and barrel (3 and 4). Cyclic compression loading profile (10 cycles) of HB femoral midshaft loaded in axial direction (C) in strain domain (F) and time domain (G). (H) Photograph series of a single axial compression cycle displayed in (F) and (G) and the corresponding percent strain. Additional characterization of HB mechanical properties can be found in the Supplementary Materials.

to buckle (Fig. 3E, 3), barrel (Fig. 3E, 4), and fracture (movie S4). Despite the fact that the solid volume fraction was only ~25% of the total HB construct functional volume (~75% from hollow interior and porous cortical walls), the 3D-printed HB femoral midshaft can support about two to three times greater mechanical loads than existing resorbable osteoconductive bone cements and press-fit osteochondral autograft (53) and approaches the stiffness and load-bearing capacity of human cortical bone (54). In addition to being both mechanically strong and stiff in the longitudinal loading direction, the HB femoral construct remained compliant and elastic under axial compressive loading (Fig. 3,

F to H), capable of rapidly undergoing numerous compression cycles (up to 25% strain) without permanent deformation (movie S4).

These highly anisotropic properties, which can be influenced by the interior pore design, illustrate that anatomically scaled HB constructs can sustain anatomical loads in one direction while remaining elastic and compliant in the orthogonal loading directions, permitting the constructs to be deformed by hand (fig. S5 and movie S4), an ideal characteristic for fitting 3D-printed bone graft into an osseous defect (5). These results indicate that HB, in addition to being translationally relevant to craniofacial and other nondirect load-bearing indications, may have potential

applications for treating defects that experience substantial mechanical loading. Like any other implant or graft surgically positioned into a defect site, however, time must be allotted to permit the region to heal, graft to integrate, and, in the case of HB, to ossify, before substantial mechanical motion and loading.

HB physical properties. Comparison of the measured dry and theoretical solid densities of HAPCL and HAPLGA fibers (the weight for a given volume if all space was filled: 90 wt % HA and 10 wt % polymer) revealed that HAPCL and HAPLGA fibers are about 50% porous (Fig. 4A and Supplementary Materials and Methods) (55). Once saturated with water, the density increases by 0.5 g/cm^3 , indicating that the porosity is open and accessible. This accessible porosity is a vital characteristic for promoting nutrient diffusion, cell migration and viability, and tissue integration. These microstructural characteristics also impart hydrophilicity and high liquid absorbency (Fig. 4B) to the HB, which is ideal for enhanced cell, bioactive factors, and nutrient infiltration. In contrast to other 3D-printed HA composite systems, which do not exhibit significant absorbance of fluids, the surfaces of HAPCL and HAPLGA are dominated by exposed HA (Fig. 4, C and D), as indicated by the dark red coloring after Alizarin Red S calcium-specific staining, a property distinct from that of HA-containing hot-melt printed scaffolds (Fig. 4E), trisolvent (1:1 HA/PLGA by weight) printed scaffolds (Fig. 4F), and even human allograft bone (Fig. 4G), which has less CaP at the surface.

Thermogravimetric analysis (TGA) (Fig. 4H) revealed that HB constructs contained as much as 15 to 20 wt % residual solvents immediately after 3D printing. These solvents are biologically toxic and must be removed before applying the HB to any biological system. Rinses with deionized water are effective at removing DCM, but not the remaining two solvents. However, a 20- to 30-min rinse in 70% ethanol not only removes all residual solvents but also has a sterilizing effect (56), although this is not a clinically approved sterilization process. Gamma irradiation is a U.S. Food and Drug Administration–approved process commonly used to sterilize polyester and CaP products before clinical use and is likely the best translational sterilization approach for HB. The TGA results validate that final, rinsed, and dried constructs, although 50% porous, con-

tain 90 wt % HA, which is the only component that does not decompose during the TGA process (horizontal dashed line in Fig. 4H).

In vitro human mesenchymal stem cell behavior on HB scaffolds

To evaluate the regenerative potential of HB, we performed in vitro experiments to assess the ability of 3D-printed HAPLGA and HAPCL scaffolds (Fig. 5, A and B) to support human mesenchymal stem cell (hMSC) adhesion and proliferation and induce osteogenic differentiation and function in the absence of osteogenic growth factors. hMSCs seeded on both HAPLGA and HAPCL scaffolds proliferated over the course of 14 days (Fig. 5, C to E) to fill the entire scaffold volume, after which time (day 28) the cell number was maintained but did not significantly increase, presumably a result of lack of space within the construct. Thus, both HAPLGA and HAPCL support human stem cell viability and proliferation. Within HAPLGA scaffolds, alkaline phosphatase (ALP) activity, an early marker of osteogenesis (57), initially decreased during proliferation but increased substantially between days 14 and 28 (Fig. 5F), as expected for cells that proliferated and then underwent differentiation once proliferation plateaued (57). Analysis of the expression of pro-osteogenic genes further supports the notion that HB promotes differentiation. hMSCs cultured on HAPLGA showed significant up-regulation of the pro-osteogenic genes, collagen type I (~15-fold increase) (58), osteopontin (~20-fold increase) (59, 60), and osteocalcin (~350-fold increase) (61) by day 28 (Fig. 5G). This was accompanied by extensive extracellular matrix (ECM) and nanocrystalline HA synthesis and deposition (fig. S6, H and I). These crystals had an atomic Ca/P ratio of 1.69 (Fig. 5H), which is similar to that of natural human bone (1.65 to 1.69) (62) and different from that of the synthetic HA used to create HB, which was measured in the same scaffolds to be 1.59. This indicates that these HA nanocrystals are likely synthesized and deposited by the cells and that HB is inherently osteoinductive.

HB in vivo biocompatibility

Although both HAPLGA and HAPCL can be successfully 3D-printed into defined structures, HAPLGA was significantly easier to print than

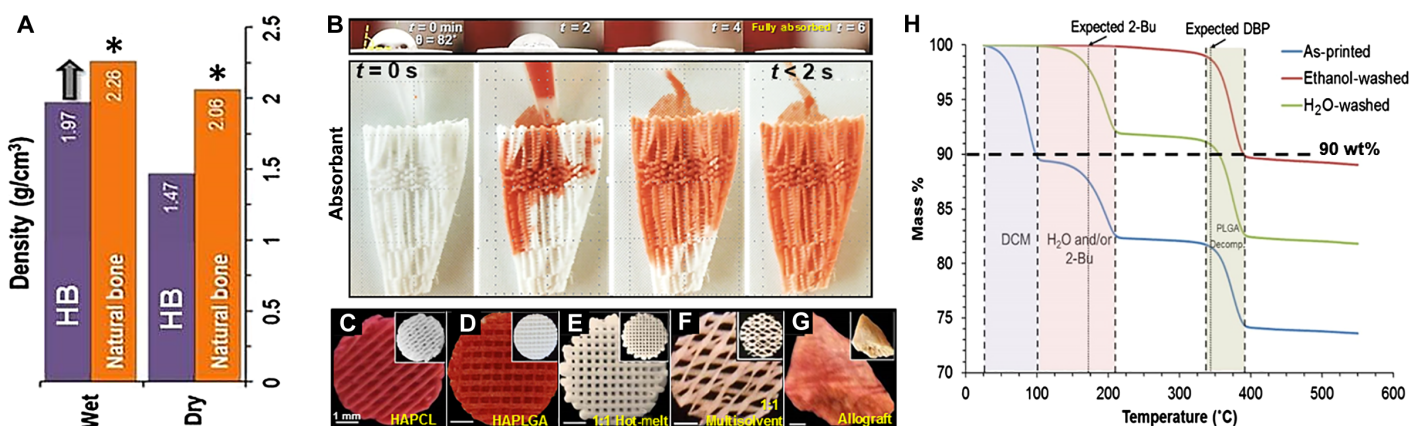


Fig. 4. Physical properties of HB. (A) Dry and wet densities of HAPCL and natural bone. Asterisk denotes value from literature (53). Upward arrow indicates that the wet density is expected to increase in vivo as water is replaced with proteins and tissues. (B) Time series contact angle profile of water on solid HAPCL surface (top) and small volume of red-colored water being injected into the end of a complex 3D-printed HAPLGA object (bottom). (C to G) Alizarin Red S–stained and Alizarin Red S–unstained

(insets) photographs of HAPCL (C), HAPLGA (D), 1:1 HA/PLGA hot-melt (E), and 1:1 HA/PLGA room temperature solvent scaffolds (F) and human cadaveric bone (G). (H) Thermogravimetric profile of as-printed, water-washed, and 70% ethanol-washed HAPLGA scaffolds. Expected evaporation or decomposition temperature ranges for individual components indicated. Note that the PLGA decomposition temperature range and the DBP boiling temperature overlap.

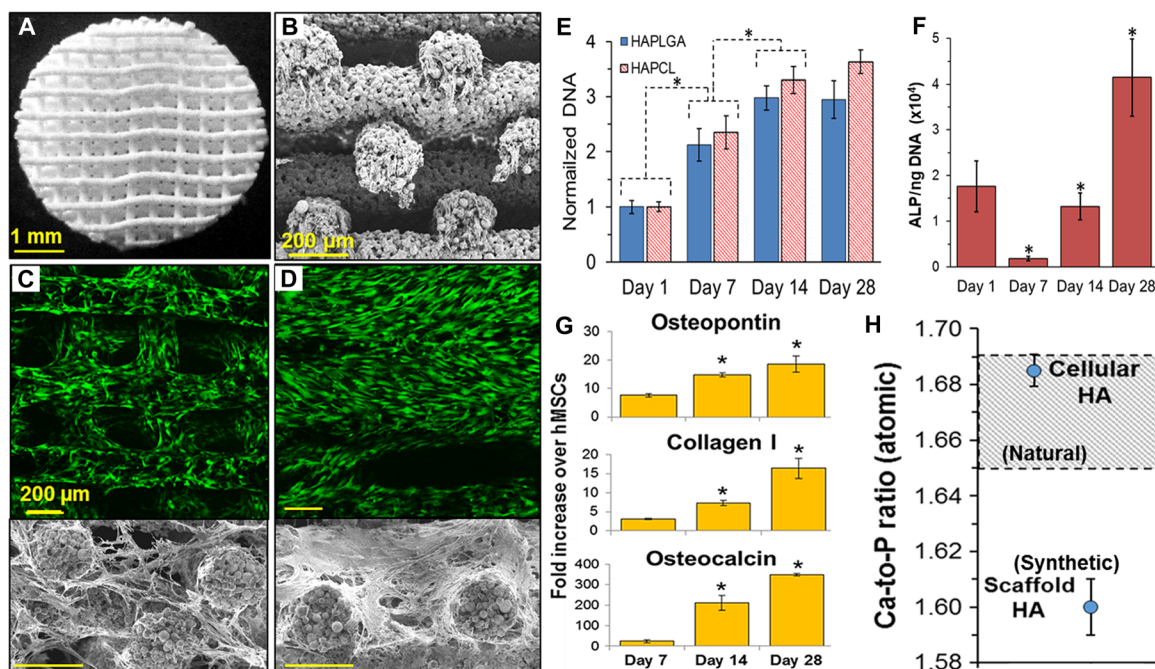


Fig. 5. In vitro evaluation of 3D-printed HB scaffolds with MSCs. Photograph of 90° offset HAPCL scaffold (A) and the corresponding cross-sectional SEM micrograph highlighting the offset architecture between layers (B). (C and D) (Top) Top-down view, laser-scanning confocal reconstructions of live (green; calcein AM) and dead (red, ethidium homodimer-1) stains. (Bottom) Corresponding cross-sectional SEM micrographs of HAPCL samples 7 days (C) and 28 days (D) after seeding with hMSCs. (E) PicoGreen quantification of DNA in HAPLGA and HAPCL scaffolds at indicated time points after seeding hMSCs. Values were normalized to average DNA measured on day 1 ($n = 3$ for all time points; error bars refer to SD). (F) ALP activity normalized to corresponding DNA content from HAPCL scaffolds at indicated time points ($n = 3$ for all time points; same samples as those used for DNA quantification; error bars refer to SD). (G) Gene expression levels of osteogenic-relevant transcripts in hMSCs grown on HAPCL scaffolds, normalized to sample-specific GAPDH (glyceraldehyde-3-phosphate dehydrogenase) values, followed by

normalization to day 0 hMSC values ($n = 3$; error bars refer to SD). (H) Atomic Ca/P measured in the HA of the scaffold itself (Scaffold HA) and of the nanocrystals within the ECM formed after in vitro culture. Gray box, Ca/P range of natural HA. (E to G) * $P < 0.05$, over previous time point for the same group. Confidence intervals (P values; two-tailed, equal variance t tests) are as follows: for DNA quantification of HAPCL samples: days 1 and 7, 0.0016; days 7 and 14, 0.013; days 14 and 28, 0.152; for DNA quantification of HAPLGA samples: days 1 and 7, 0.0032; days 7 and 14, 0.043; days 14 and 28, 0.862; for ALP/ng DNA of HAPCL samples: days 1 and 7, 0.034; days 7 and 14, 0.0026; days 14 and 28, 0.0053; and for fold increase in gene expression of HAPCL samples: osteopontin: days 7 and 14, 0.00041; days 14 and 28, 0.00026; collagen I: days 7 and 14, 0.0033; days 14 and 28, 0.017; osteocalcin: days 7 and 14, 0.0049; days 14 and 28, 0.050. Additional in vitro related figures for hMSCs seeded onto 30° advancing angle HB scaffolds can be found in the Supplementary Materials.

HAPCL, specifically in fabricating large (many dozen layers) objects as well as conforming to tight, organically shaped contours. HAPLGA also had superior mechanical properties and could be elastically strained upward of 60% (tensile) and 50% (compression); HAPCL, in contrast, could strain upward of 35% (tensile) (fig. S3B) and 50% (compression). For these reasons, we evaluated the in vivo biocompatibility and osteogenic function of HAPLGA; however, because PCL has been extensively used in the bone and tissue engineering field (43), it is a reasonable assumption that HAPCL would show similar biocompatibility in vivo, although long-term degradation times would likely vary from HAPLGA.

To examine biocompatibility in vivo, we subcutaneously implanted HAPLGA scaffolds (that is, HB) in female BALB/c mice. HA/PLGA (1:1) hot-melt scaffolds were also implanted as a comparison, because they are similar to materials that have been previously used and evaluated as bone implants (32). After 7 days, tissue had already begun to infiltrate and vascularize throughout the HB scaffolds (fig. S7A). The hot-melt scaffold explants could not be histologically processed successfully, a result of their highly brittle nature and the dissolution of the PLGA (majority scaffold component) in histological process solvents,

which caused the loss of integrated tissues and embedded HA particles during processing (Fig. 6F). After 35 days in vivo, the HB scaffolds were completely integrated with the surrounding host tissue (Fig. 6, A to C). SEM imaging of explanted scaffold tissues revealed that, in both material systems, the tissue formed intimate contact with the material within and throughout the scaffold volume by day 35. However, there was a distinct difference in the structure and texture of the tissue within HB (Fig. 6, D and E) compared to that within the hot-melt printed scaffolds (Fig. 6, G and H). Tissue surrounding HB more closely mimicked healthy ECM, with defined collagenous ECM (fig. S8) and blood vessels ranging from 2- μ m single-cell capillaries to multihundred-micrometer vessels present throughout the scaffold (Fig. 6, B to D, and fig. S8). In contrast, the tissue within the 1:1 HA/PLGA hot-melt scaffolds was characteristically dense and relatively acellular compared to the HB counterparts (Fig. 6, G and H). SEM imaging also revealed a population of unhealthy blood cells (burr cells) inhabiting the tissue within the 1:1 HA/PLGA scaffolds (Fig. 6I), which may indicate a strong local fibrotic response. Additional staining with Alizarin Red S did not indicate any obvious mineralization within the integrated tissues by day 35 (fig. S7C); however, because there was no

source of osteoprogenitor cells in this subcutaneous model, *de novo* mineralization was not expected.

HB efficacy in a rat spinal fusion model

To assess the capacity of HAP/LGA HB to induce bone regeneration in a preclinical *in vivo* model, we evaluated HB scaffolds with and without incorporated recombinant human bone morphogenetic protein 2 (rhBMP-2) in a previously described rat posterolateral spinal fusion (PLF) model (63, 64). The PLF model was chosen because it replicates the spinal fusion procedure in humans, and it is widely accepted to assess and predict regenerative potential in the spinal fusion setting (65). Although the amount of osteoinductive stimulus necessary to achieve fusion is different in the rat than in the human (primarily because of the difference in anatomical size), it is useful because it is cost-effective and reproducible, with established positive and negative controls (66).

HB scaffolds were implanted bilaterally at the L4 and L5 transverse processes, which had been decorticated immediately before. As a control, an equivalent amount of HA powder (42 mg, identical source and mass of HA that was used to create each HB scaffold) was implanted. A demineralized bone matrix (DBM) scaffold in sheet form (Bacterin) was also used as a control, because DBM scaffolds routinely elicit a 50 to 60% per-animal fusion rate in this model (64). Autografts promote spinal fusion in humans and, when used in higher-order animal models, elicit fusion rates of ~50%; autografts are not used as standard positive or com-

parative controls in the rat PLF model, however, because the limited volume of obtainable bone is insufficient to reproducibly promote successful fusion (67). Radiographic imaging of each spine shows placement of the scaffolds at the L4 and L5 transverse processes (Fig. 7A). Scaffold placement relative to spinal features can be also observed in the gross photograph of a spinal column cross section explanted after 4 weeks *in vivo* (Fig. 7B); after 4 weeks *in vivo*, the HB scaffolds became infiltrated by and integrated with the surrounding tissue.

After 8 weeks *in vivo*, scaffolds and surrounding tissues were explanted and evaluated for fusion as well as for new bone formation via manual palpation and laboratory synchrotron-based micro-computed tomography (microCT), respectively. The mean fusion score of the HB group was significantly higher than that of a collagen scaffold historical control (1.2 versus 0) (63), as well as the HA powder control, which also had a mean fusion score of 0. Moreover, the mean fusion score of HB group was statistically equivalent to that achieved with a DBM control scaffold (1.2 versus 0.7; Fig. 7C). The fusion rate (as determined by the number of sides successfully fused, with two sides possible per animal) was also significantly higher in the HB group relative to the collagen historical negative control and HA powder groups (46% versus 0 and 0%) and was comparable to the DBM group (25% of sides successfully fused; Fig. 7D). These results indicate that the HB scaffold has intrinsic osteoinductive capacity sufficient to induce bone regeneration and successful spinal fusion in the rat without any added growth factors and shows similar

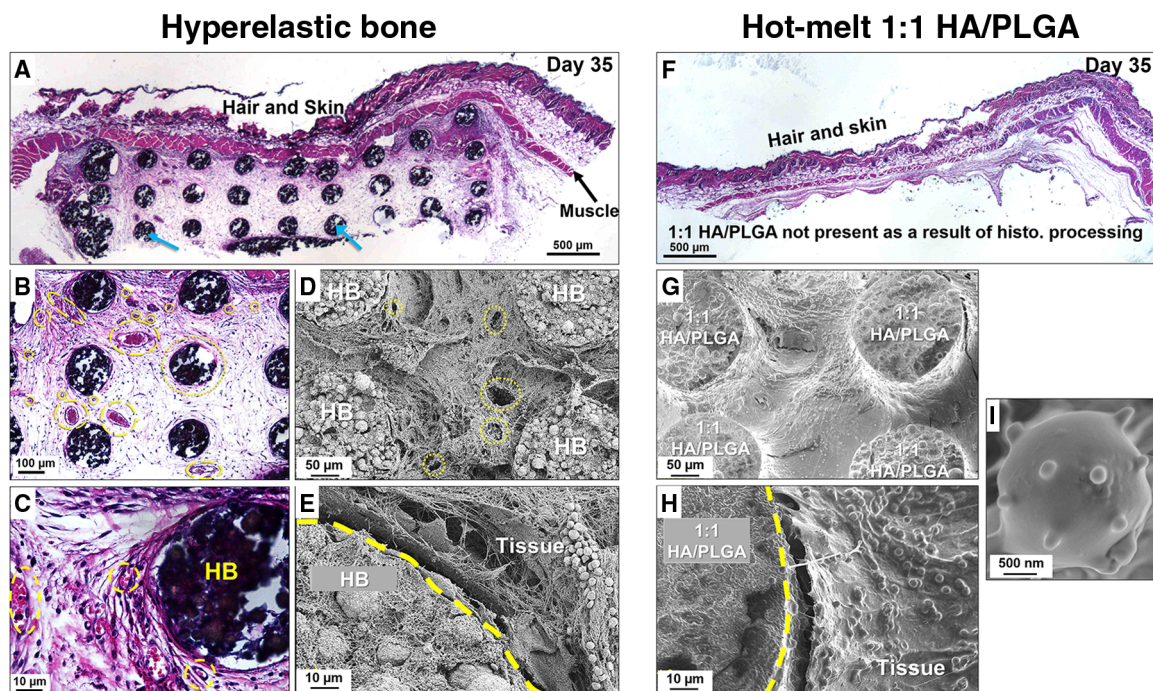


Fig. 6. Biocompatibility evaluation *in vivo* with a mouse subcutaneous implant. (A) Gross hematoxylin and eosin (H&E) histological image of day 35 HB explant cross section. Blue arrows, HB fiber cross sections. The densely packed HA particles within the HB stain dark purple to black. (B and C) H&E histological image of day 35 explant with HB fiber cross sections (dotted yellow circles), vessels (dashed yellow circles), and capillaries (solid yellow circles). (C) Higher-magnification section of (B). (D) SEM micrograph of day 35 explanted HB scaffold. Several vessels are indicated by dotted yellow circles; soft tissue completely fills the space between the HB fibers. (E) Higher-magnification SEM micrograph of (D) highlighting the structure of HB, new tissue, and the HB scaffold-

tissue interface (dashed line). (F) Gross H&E histological image of day 35 hot-melt 1:1 HA/PLGA-explanted scaffold. Because of the solubility of PLGA in common histological solvents, and given that more than half the scaffold volume is composed of PLGA, the 1:1 HA/PLGA scaffold materials and incorporated tissues did not survive histological processing. (G) SEM micrograph of the cross section of day 35 hot-melt 1:1 HA/PLGA-explanted scaffold and tissue. No vessels are visible. (H) Increased magnification SEM micrograph of (G) illustrating the hot-melt HA/PLGA-tissue interface (dashed line). (I) Representative burr cell; these were found throughout the tissue within the hot-melt 1:1 HA/PLGA-explanted scaffold. Additional related figures can be found in the Supplementary Materials.

osteogenic capacity not only to the DBM used here but also to other commercially available DBMs that have been evaluated in this animal model (64). We also found that HB can serve as an effective carrier for the delivery of rhBMP-2. When HB scaffolds (~45 mg) were preloaded with 1.5 μg of rhBMP-2 (0.003% loading by scaffold weight), the mean fusion score was significantly higher than that of the HB alone group (1.8 ± 0.4 versus 1.0 ± 0.7 ; Fig. 7C), and the fusion rate was similarly elevated (83% versus 46%; Fig. 7D).

The host bone volume in the L4 and L5 transverse processes was quantified in four control animals outside of the study groups and averaged ($267 \pm 32 \text{ mm}^3$) using laboratory microCT. The volume of new bone formed around the HB scaffolds was calculated by subtracting scaffold volume from total bone plus scaffold volume for each left and right implant region in each animal. This resulting value for total bone volume was evaluated against historically determined, natural mean bone volumes for rats of the same strain, age, and weight range. The new bone volume data illustrate that HB alone induces substantial new bone formation, and the rhBMP-2-carrying HB significantly induces more than HB alone ($19.5 \pm 6.3 \text{ mm}^3$ versus $38.9 \pm 11.4 \text{ mm}^3$; Fig. 7E).

High-resolution, synchrotron microCT analysis of HB samples without and with rhBMP-2 revealed that there was substantially more bone formation both around the exterior and throughout the interior of the HB + BMP scaffolds compared to the scaffolds without added rhBMP-2; however, new bone formation within the HB scaffolds without BMP was still apparent (Fig. 7, F and G, and movie S5). These results demonstrate that 3D-printed HB is osteogenic but may be optionally enhanced through addition and absorption (Fig. 4B) of established growth factors, such as BMPs (68–70). Not only is the material as efficacious as DBM, but it is more widely available and substantially cheaper and easier to process and fabricate into complex and patient-specific shapes relative to DBM, which is in limited supply, carries risks for disease transmission, and is subject to variability in efficacy due to the differences in allograft sources.

HB efficacy in a large primate calvarial bone defect

Our biocompatibility and spinal fusion studies in mouse and rat models, respectively, revealed that there is no adverse host response to HB (as would be expected on the basis of its composition) and that HB can

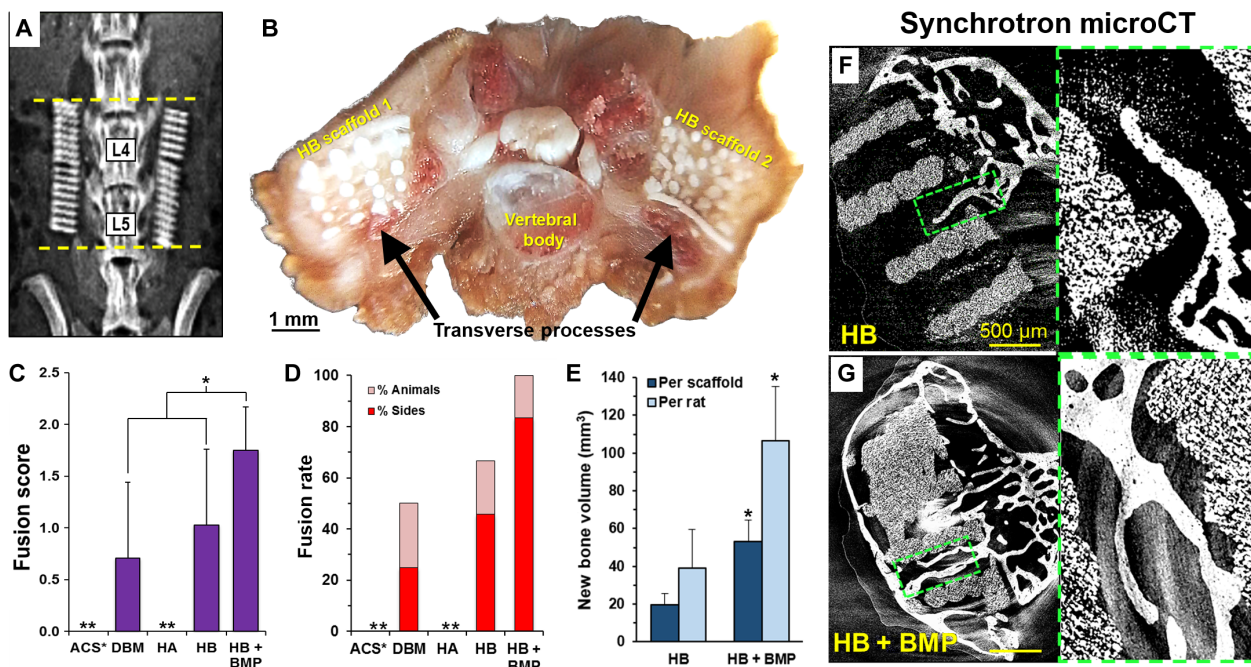


Fig. 7. Evaluation of HB in vivo for rat spinal fusion. (A) Representative radiograph illustrating bilateral placement of HAPLGA (HB) scaffolds across the L4 and L5 vertebral body transverse processes. (B) Photograph of the cross section of rat spinal column containing HB scaffolds 4 weeks after implantation. Placement of HB scaffolds on transverse processes (black arrows) is visible, as is significant tissue incorporation into the scaffolds. (C) Fusion scores of spinal segments with scaffolds explanted after 8 weeks. An established scoring system for the fusion score was used, whereby 0 = no bridging bone, 1 = unilateral bridging bone, and 2 = bilateral bridging bone. ACS, absorbable collagen sponge (historical control); DBM, demineralized bone matrix; HA, hydroxyapatite granules; HB, HAPLGA; HB + BMP, HAPLGA preloaded with 1.5 μg of rhBMP-2 before implantation. (D) Fusion rates were calculated as both percent sides fused (two sides per animal) as well as on a per-animal basis [$n = 6$ for ACS, DBM, HA, HB + BMP groups; $n = 12$ (two $n = 6$ replicates) for HB group]. For the

latter, unilateral bridging bone was considered successful fusion (fusion score of ≥ 1.0). (E) Laboratory microCT-based quantification of new bone volume within and surrounding the HB scaffolds (with and without 1.5 μg of rhBMP-2 per scaffold). $n = 6$ animals for all groups. (F and G) Representative single-slice synchrotron microCT images of the cross section of HB scaffolds without (F) and with (G) rhBMP-2 added. Green rectangles, region enlarged at right; bright white, native bone; speckled black-white, HB scaffold. Error bars for (C) and (E) refer to SD. Confidence intervals (P values; two-tailed, equal variance t tests) for groups shown in (C) are as follows: HB/HB-BMP, 0.0036; DBM/HB-BMP, 0.0004; HB/DBM, 0.21. Confidence intervals (P values; two-tailed, equal variance t tests) for groups shown in (E) are as follows: per-scaffold HB/HB-BMP, 0.00003; per-animal HB/HB-BMP, 0.0003. $*P < 0.05$, between indicated groups or when compared with previous time point for the same material group. The double asterisk (**) indicates a value of 0 (no fusion or newbone formation was observed).

perform just as well as naturally derived bone matrix in eliciting new bone growth. These results are from idealized small rodent model systems, in which the necessary scaffold architectures were predetermined before implantation and were small in size relative to those required for humans. Actual clinical scenarios are rarely so ideal and require the surgical team to adapt to evolving circumstances and new information. This includes acquiring, modifying, and implanting the required materials in defects that may vary widely in size and shape.

We therefore implemented HB in a case study within a large primate calvarial defect. The research primate, a rhesus macaque (*Macaca mulatta*, 11.65 kg), had been the subject of studies requiring several cycles of subcortical, brain-interfacing electrode implantation and removal, ultimately resulting in a large region of weak, unhealthy cranial cortical bone that was in need of repair. Because the true size and geometry of the defect site would not be known until the site had been cleared and the abnormal bone had been removed, an extra large HB construct (40 × 40 × 4 mm) was fabricated (Fig. 8A) that could be trimmed and altered intraoperatively immediately before implantation to fit the defect site (Fig. 8B). To emulate cortical bone, the construct consisted of 13 layers, with the top and bottom layers being solid and the interior 2 to 12 layers being highly porous (Fig. 8A, inset), to permit surrounding tissue to integrate with the HB construct. A 120° advancing angle pattern was chosen to ensure homogeneous, lateral mechanical properties along the implant perimeter loading directions. Additional details regarding calvarial implant design and surgical procedure may be found in the Supplementary Materials.

After 4 weeks, the site was exposed (Fig. 8C) to place a new electrode array under the implanted HB. We found that soft, vascularized tissue was covering and connected with the extracranial surface of the HB construct. During the first attempt to remove the HB implant, the solid, extracranial HB construct surface was delaminated, revealing an interior that had become highly integrated with the surrounding tissue. It was not expected that the HB implant would have integrated so well with the surrounding tissue after only 4 weeks, which prevented easy separation from the surrounding native bone. A craniotomy that included a 1- to 3-mm perimeter of native bone tissue around the HB construct was performed, freeing the HB calvarial construct (Fig. 8C).

Closer examination of the explanted, chemically fixed sample using optical microscopy (Fig. 8, D to F) revealed that native tissue had integrated throughout the volume of the HB implant (Fig. 8, E and F) and that the skull-HB interface was essentially seamless. Small vessels were also observed immediately under the HB material comprising the intracranial surface (Fig. 8D) and were advancing from the surrounding native bone tissue toward the center of the implant. The surfaces and outer perimeter of the HB explant physically felt much harder than the HB material before implantation. This qualitative observation is similar to that made for the rat spine HB explants. Mechanical compression testing of small sample specimens derived from an as-printed, chemically fixed HB control (“1”), natural bone near the bone-HB interface (“2”), HB near the bone-HB interface (“3”), and HB near the geometric center of explant (“4”) revealed that the mechanical properties of the HB changed substantially after 4 weeks in vivo. The stress-strain behavior of regions 2 and 3 were nearly identical (Fig. 8G) and distinct from the preimplanted material (1) and HB in the center of the explant, indicating that the HB material nearest to the native bone was at least beginning to ossify by 4 weeks. The lower stiffness of the material from region 4 was likely the result of local degradation of the PLGA as new tissue was just beginning to infiltrate and remodel the region. Histological (Fig. 8, H to

K) and synchrotron microCT (Fig. 8, L and M) analysis of portions of the explant revealed intimate interfaces between the native bone and HB as well as new integrated soft tissue and HB (Fig. 8, L and M). New woven bone could be observed advancing into the HB implant space from the native bone (Fig. 8I) in addition to heavy vascularization within the HB implant interior (Fig. 8J). Although substantial ossification and mineralization was not expected by 4 weeks, there was some evidence of new mineralized tissue within the HB implant (Fig. 8L), which appeared to be either advancing into or emerging from the interior of an HB strut (Fig. 8M). This region was not in direct contact with the native bone. These data, along with the in vitro results showing the up-regulation of osteogenic gene expression of hMSCs without the addition of osteo-inducing factors, indicate that HB itself may have some osteoinductive potential.

Although this is a singular case, this particular defect in the rhesus macaque represents a translational analog for human applications and demonstrates the following: (i) the surgical application of HB on a larger, translationally relevant scale; (ii) the ability to digitally customize the design to be 3D-printed and rapidly produce that design to fit the “patient”-specific defect; (iii) the ability to manipulate the HB material in situ by cutting to size and press-fitting into the defect site without the need for additional mechanical fixation or stabilization; and (iv) the ability to induce significant and rapid tissue integration with surrounding host tissues on clinically relevant scales, without any adverse biological response or infection.

DISCUSSION

There is a substantial, ongoing, global medical need for osteogenic bio-materials that are not only highly efficacious but also easy to surgically implement, cost-effective, and capable of being manufactured on scales that can address this widespread need. With HB, we have demonstrated that well-established, safe, clinically used medical materials (PLGA/PCL and HA) can be processed to create new composite material systems with unique mechanical, physical, and biological properties and that these new systems can potentially be synthesized and manufactured at scales and speeds that are clinically relevant, using purely synthetic materials that are substantially less expensive than cadaver-derived allografts (DBM). The capacity for this material to be fabricated into the required geometry and size, with precision internal architecture, is certainly an advantage of the 3D printing process, making it promising for patient-tailored implants; however, it is the mechanical and physical properties of the resulting 3D-printed HB material, which, unlike other ceramics or ceramic-dominated polymer-ceramic composites, can be intraoperatively manipulated (via cutting, rolling, folding, suturing, etc.), making HB a surgically relevant and easy to implement material. Through in vitro studies, without any addition of osteo-inducing factors in the medium, HB can stimulate a significant osteogenic response in clinically relevant adult hMSCs. The in vivo mouse subcutaneous study revealed that HB is biocompatible and elicits better tissue growth and structure than the commonly implemented hot-melt polymer-CaP composite materials, whereas the rat PLF studies showed that HB is just as efficacious at promoting bone growth as allograft-derived DBM. In addition, HB is a singular base material, which can be further augmented through incorporation of chemical or biochemical species directly into the 3D inks before 3D printing or absorbed into the 3D-printed constructs before implantation. The final case study that involved HB’s implantation in a calvarial bone defect in a rhesus macaque demonstrated that HB can be quickly produced on a relevant scale and fashioned intraoperatively to closely fit

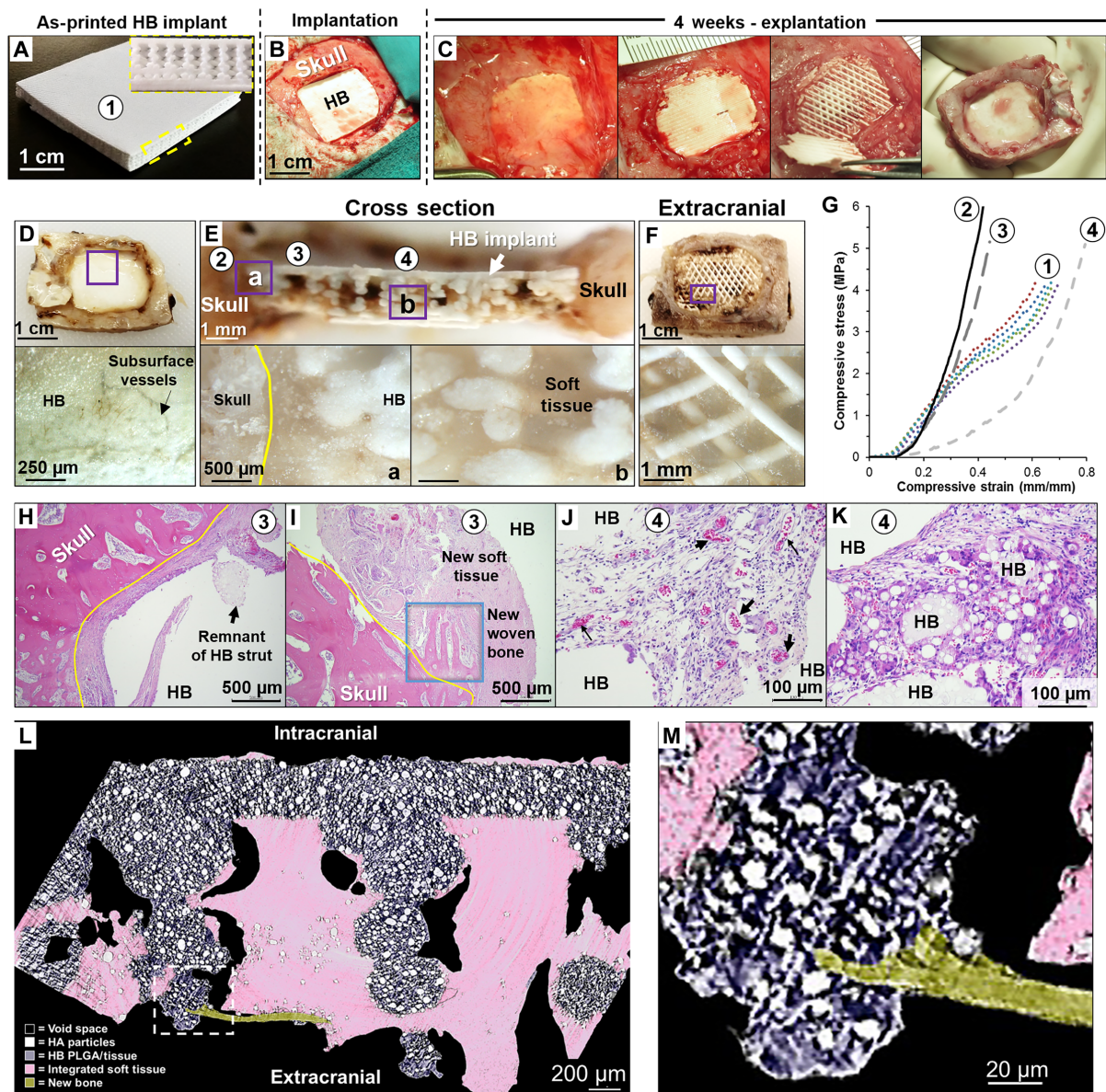


Fig. 8. HB as a macaque calvarial defect bone graft. (A) Photograph of $40 \times 40 \times 4$ -mm 3D-printed HAP/LGA (HB) bone graft. The top and bottom layers of the construct are solid, whereas the sides and interior are porous (inset). (B) Photograph of trimmed HB construct from (A) after implantation into ~ 2 cm across the calvarial defect site. (C) Photograph series of the HB graft and defect site 4 weeks after implantation, and the resulting cranial-HB explant. Note that, during explantation, the extracranial-oriented solid HB surface peeled away from the rest of the construct. (D) Photographs showing (top) intracranial surface of the cranial-HB explant and the corresponding micrograph (bottom) of the surface of the HB graft indicated by purple box. Small vessels emanating from the native tissue on the exterior of the HB graft under the thin surface of the HB graft (arrow). (E) Photographs of gross cross section (top) and the corresponding optical micrographs (bottom) highlighting the cranial graft interface (region a) and the center of graft (region b). (F) Photograph (top) showing the extracranial surface of the cranial-HB explant and the corresponding micrograph (bottom) of the surface of the HB graft indicated by purple box. (G) Mechanical compression results of 4-mm-diameter biopsies taken from the corresponding numbered regions in (E) as well as from the as-printed bone graft in (A) (1) before implantation. The four samples from region 1 were samples from across the width of the $40 \times 40 \times 4$ -mm graft.

(H) Decalcified H&E histograph of cortical bone from calvarium at site of attachment of the scaffold (region 3), with associated fibrovascular proliferation (yellow line). A small portion of the scaffold survived the decalcification and histological processing (black arrow). (I) New woven bone (blue square) and associated fibrovascular connective tissue along the periosteal surface (region 3) of the cortical bone (yellow line). (J) Evidence of significant soft tissue infiltration and vascularization (arrows) within the interior of the HB scaffold (region 4). (K) Fibrovascular proliferation and associated inflammation composed of macrophages, lymphocytes, and plasma cells within region 4. (L) A false color single slice of synchrotron microCT reconstruction from the rhesus macaque 4-week HB calvarial explant, depicting an area between regions 3 and 4 from (E). The explant is characterized by significant soft tissue (pink) integration, including intimate growth along the edges and into the HB material. Large void spaces between the tissue and the HB within the construct are likely artifacts from the chemical fixation and dehydration procedure after explantation. (M) A possible early-stage new osseous tissue is present (yellow/brown) emerging from or extending into an HB fiber [detail of the box surrounded by dashed white line is in (L)]. Grayscale, contrast-defined reconstructed slices can be found in the Supplementary Materials (fig. S9).

the defect site. In a short period of time (4 weeks), the HB implant promoted rapid tissue integration within the defect space with signs of mineralization. The value of HB's technical and medical advantages is further enhanced through its capacity to be rapidly manufactured into small or large, simple or complex, porous constructs via simple, room temperature extrusion-based 3D printing of instantly drying 3D ink. These qualities mark HB as a promising new synthetic bone graft biomaterial with substantial translational potential, to be confirmed in comprehensive, indication-specific, large animal model studies to evaluate HB's efficacy for specific orthopedic and craniofacial indications.

MATERIALS AND METHODS

Study design and reproducibility

Mouse subcutaneous implant study. Sample size ($n = 3$ animals, two implants per animal) for each of two time points was determined on the basis of our previous studies with 3D printable biomaterials developed in our laboratory. This study was intended to be primarily qualitative (histological evaluation of possible inflammation and immune response) and to serve as a biocompatibility check before moving onto more complex, functional, specific studies and to compare the new HB material with previously published hot-melt 3D-printed HA-polymer composites. We did not alter the number of animals over the course of the study. Final end points were determined before study initiation and were based on the established end point of 7 and 35 days to determine short- and long-term immunological responses, if any. It was determined before study initiation that all explanted scaffolds would be histologically analyzed and imaged using SEM, with the exception of animals that required euthanasia before the study end point due to illness or other unforeseen condition. Here, no animal required euthanasia before the study end point. This study was not randomized or blinded because the two scaffold groups (HB and hot-melt printed HA/PLGA) were substantially different in terms of appearance, handling (soft versus hard), and required different histological process approaches (ultimately, unsuccessful for the hot-melted printed scaffolds).

Rat posterolateral fusion study. From a previous work (63), power analyses showed that 12 measurements per group are required to obtain 80% power with an effect size of 0.72. Because we performed bilateral fusion, each side of the spine represented one measurement, with each side assessed for fusion independently. This required a minimum of six animals per treatment group. The HB-treated condition was repeated in a follow-up study (also $n = 6$) to confirm the efficacy of bringing the total sample size for this group to $n = 12$ (all other groups were $n = 6$). The final end points were determined before study initiation and were based on the well-established end point of 8 weeks postoperative for the rat PLF model. It was determined before study initiation that all spinal fusion data from each animal would be included, with the exception of animals that required euthanasia before study end point due to illness or other unforeseen condition. Here, no animal required euthanasia before the study end point, and data from every animal were included in the analyses. No outliers were expected or predefined, and as such, no outliers were excluded from this study. This was an *in vivo* study that took place over a period of several months. Although it was only performed one time, conditions were equalized to the best of our ability and that of our animal care facility. The objectives of this work were to compare the spinal fusion capacity of the HB scaffold relative to comparative controls and to determine the capacity of the HB scaffold to serve as a carrier for

a biologic (rhBMP-2). Sprague-Dawley rats were used in these studies. The rat spinal fusion model is a well-established preclinical model for proof-of-concept work validating materials as bone graft substitutes. This was a controlled laboratory experiment in which various scaffold materials were implanted in the rat to compare their relative capacities to elicit spinal fusion. The ability of the experimental scaffold (HB) to promote successful fusion was compared against that of a DBM scaffold, which is known to be osteoinductive and osteoconductive, and was expected to achieve fusion at a rate of 50%. It was also compared against an equivalent amount of HA particles present in the HB (but unprinted), to control for the intrinsic osteoinductivity or osteoconductivity of the HA particles present in the HB. The HB was also evaluated when applied in the PLF model as a carrier for growth factor (that is, a biologic). Animals were randomly assigned to one of each of the treatment groups in this study. All animals were purchased from Charles River in one order and arrived in our institution's animal facility at the same time. Randomization was based on the arbitrary number assigned by our facility's census system. The data from this study were collected and processed randomly, as is required to execute the blinded palpation for fusion scoring that is standard for this animal model. The study was blinded, and the method used for allocation of concealment was the construction of a key with animal IDs linked to numbers determined by a research randomizer program. The animal caretakers were not privy to identifying data. The identifying data and key were stored on a server in a separate place from the blinded IDs and were not accessed by the investigators or any other study staff until the data were obtained and ready for analysis.

Detailed experimental methods

HB 3D ink and additional 3D printing material preparations. HB inks were synthesized by thorough mixing of PLGA (82:18) copolymer (Boehringer Ingelheim) or PCL ($M_n = 70,000$ to 90,000; Aldrich), ceramic powder, and a mass mixture of DCM (Sigma), 2-Bu (Sigma), and DBP (Sigma) in a ratio of 10:2:1. 2-Bu (0.6 g) was used for every 1 cm³ of HA powder (20 to 30 μm ; Sigma). The inks are periodically stirred in an open environment to increase the viscosity through solvent evaporation until it reaches an empirically determined viscosity ideal for 3D printing (low shear stress viscosity of 30 to 35 Pa·s; fig. S2A). Single-solvent inks were made similarly but only by using DCM as the solvent. HAPLGA and HAPCL inks were rheologically characterized using a Couette fixture with solvent trap (MCR Rheometer, Paar Physica) under rotational shear at interval stresses between 0 and 100 Pa. Materials for hot-melt 3D printing were prepared by combining and thoroughly mixing sieved (<100 μm) PLGA or PCL powder with HA powder in 1:1 by mass ratio and allowed to heat at 200°C for 60 min. All printed structures were fabricated using EnvisionTEC 3D-Bioplotter.

hMSC *in vitro* culture on HB. Passage 2 female hMSCs (Lonza) were expanded up to passage 5 using MSC basal medium and proliferation kit (Lonza) according to the manufacturer's instructions. Cylindrical 5-mm-diameter, 10-layer-thick (2 mm) HAPLGA and HAPCL scaffolds were punched from 1.5 × 1.5-cm square 3D-printed sheets using a 200- μm -diameter nozzle into a 90° offset advancing angle architectures with 300- μm spacing between parallel fibers within the same layer (Fig. 6, A and B). Before cell seeding, HB scaffolds were rinsed in 70% ethanol for 30 min, followed by three 4-min rinses in sterile phosphate-buffered saline (PBS). hMSCs (150,000) were seeded into each scaffold via injection of 10- μl cell suspensions in proliferation medium composed of 1× low-glucose Dulbecco's modified Eagle's medium modified with 10% fetal bone serum, Hepes buffer, L-glutamine, and 10 U of antibiotic-antimycotic

(Invitrogen). A portion of this medium (500 μ l) was added to each well 1 hour after initial seeding. All cell-seeded samples were incubated at 37°C in 5% CO₂.

Mouse in vivo subcutaneous implants. All animal work was performed under a protocol approved by the Institutional Animal Care and Use Committee (IACUC) at Northwestern University and conducted in accordance with IACUC policies and procedures. For mouse subcutaneous implant studies, 5-mm-diameter, 10-layer-thick (2 mm) scaffolds having an open 0° to 90° pore pattern were produced using a 200- μ m nozzle and ~300- μ m spacing between adjacent parallel fibers. Female BALB/c mice were anesthetized using inhalational isoflurane. A subcutaneous incision (6 mm) was made on the back of each mouse, near the nape of the neck. A HAPLGA scaffold was inserted under the skin and pushed to the left side of the incision. A HA/PLGA (1:1 by mass) hot-melt scaffold was inserted through the same incision and pushed to the right side of the incision. Mice were sacrificed at 7 and 35 days after implantation ($n = 3$), at which point scaffolds and surrounding tissues were removed and prepared for analysis.

Rat in vivo PLF. For rat PLF studies, 24 female Sprague-Dawley rats (12 to 16 weeks old) were randomly assigned to one of four treatment groups: (i) HAPLGA without rhBMP-2, (ii) HAPLGA preloaded with 1.5 μ g of rhBMP-2, (iii) equivalent mass HA powder (not 3D-printed), and (iv) DBM sheet scaffold (not 3D-printed, included as a comparative control), with an $n = 6$ per group. An additional $n = 6$ HB study group was evaluated separately and independently under the same sample, experimental, and surgical conditions, resulting in a total of $n = 12$ (two separate $n = 6$ studies) for HB. To evaluate spinal fusion capacity of the HAPLGA, 2 × 2-cm HAPLGA squares (0° to 90° alternating angle, 500- to 700- μ m pore size), composed of ten 300- μ m-thick layers, were 3D-printed, washed in 70% ethanol and sterile PBS, and manually cut into 1.5 × 0.3 × 0.3-cm rectangles. For HAPLGA preloading, a 20- μ l solution of 1.5 μ g of rhBMP-2 in normal saline was applied to each scaffold, distributed uniformly along the pores using a pipette. Two scaffolds were prepared per animal and allowed to rest at room temperature in a sterile tissue culture hood for a period of 30 min before implantation to facilitate evaporation of excess liquid.

Rats were anesthetized under continuous inhalational isoflurane at a dose of 2 to 3% in 100% oxygen. Using our previously described surgical technique (63, 64, 71), we made a posterior midline incision over the lumbar spine, followed by two separate fascial incisions 4 mm from the midline. The transverse processes of L4 and L5 were exposed using a muscle-splitting approach via blunt dissection down to the periosteum. The surgical site was irrigated with gentamicin, and a high-speed burr was used to decorticate the exposed transverse processes. Scaffolds were then implanted bilaterally in the paraspinal musculature, bridging the L4 and L5 transverse processes. Fascia and skin were closed using 3-0 monocryl sutures and wound clips, respectively; the latter were removed 7 to 10 days postoperative. After surgery, rats were individually housed and allowed to eat, drink, and bear weight ad libitum.

Rhesus macaque in vivo calvarial defect

A rhesus macaque (*M. mulatta*, 11.65 kg) that had previously received two right cortical array implants was anesthetized with ketamine/midazolam induction and kept under isoflurane general anesthesia during the surgical procedures. The bone defect was exposed through a midline incision, and the connective tissue around the defect site was dissected and removed. The defect void space was extended on all side with rongeurs by about 1 to 1.5 mm. This provided a fresh, healthy bone edge and

more exposure to remove the implanted array. The 40 × 40 × 4-mm HB construct was trimmed to fit snugly into the craniotomy and was pushed into place. The area was flushed thoroughly with saline before closing the incision using vertical and horizontal mattress sutures. Four weeks after implantation, an incision was made in the skin in the same location as the previous incision, followed by blunt dissection and cleaning of the scalp surface. The HB graft was identified and removed along with a perimeter of 1- to 3-mm-thick cortical bone. This explanted HB calvarial construct was rinsed with PBS and chemically fixed for 1.5 weeks in 10% neutral buffered formalin, after which it was used for the photographs, mechanical testing, histology, and synchrotron microCT-derived images, and data that are presented in Fig. 8.

All animal work and protocols used in this research followed the National Institutes of Health *Guide for the Care and Use of Laboratory Animals* and were previously approved by IACUC at Northwestern University. Animal care was administered under the guidance of the Northwestern Center for Comparative Medicine.

Statistical analysis

Unless otherwise noted, all statistical analyses were performed using equal variance, two-tailed *t* tests. Error bars are given as SDs, and sample group sizes are given in the respective figure caption(s) or Materials and Methods section(s).

SUPPLEMENTARY MATERIALS

www.sciencetranslationalmedicine.org/cgi/content/full/8/358/358ra127/DC1
Materials and Methods

Fig. S1. Additional functionalities and potential applications of 3D-printed HB.

Fig. S2. Microstructure of 1:1 HA/PLGA hot-melt 3D-printed composite.

Fig. S3. Additional rheological and mechanical properties of HB.

Fig. S4. Origin of HB's mechanical properties and additional mechanical data.

Fig. S5. Axial compressive loading of HB femoral section by hand.

Fig. S6. Additional in vitro results: hMSCs seeded onto 30° advancing angle HAPCL scaffolds.

Fig. S7. Additional mouse subcutaneous implant in vivo results 7 and 35 days after implantation.

Fig. S8. Additional in vivo SEM micrographs of HB scaffolds explanted 35 days after being subcutaneously implanted into a mouse.

Fig. S9. Contrast-enhanced grayscale (non-false-colored) version of Fig. 8 (L and M).

Movie S1. A 32x speed movie of HAPLGA ink being 3D-printed into 14-cm-tall, 6-mm-diameter cylinder composed of hundreds of layers, followed by a 64x speed movie illustrating HAPLGA being 3D-printed into 7.5-cm-tall double helix modeled after the structure of DNA.

Movie S2. 3D printing and physical manipulation of HB (HAPLGA) sheets.

Movie S3. HA/PLGA (1:1) hot-melt 3D-printed object being impacted and shattered by a hammer, followed by 3D-printed HAPLGA undergoing a series of hammer impacts and bouncing back.

Movie S4. Longitudinal compression, axial cyclic, and finger compression of hydrated 3D-printed HB femoral midshafts shown in Fig. 3.

Movie S5. Synchrotron microCT of 8-week PLF-explanted HAPLGA (HB) scaffolds (black and white speckled object in the movie), without and with 3 μ g of rhBMP-2 added, illustrating new bone (dense white) material within and around HB.

REFERENCES AND NOTES

1. A. Oryan, S. Alidadi, A. Moshiri, N. Maffulli, Bone regenerative medicine: Classic options, novel strategies, and future directions. *J. Orthop. Surg. Res.* **9**, 18 (2014).
2. S. V. Dorozhkin, Bioceramics of calcium orthophosphates. *Biomaterials* **31**, 1465–1485 (2010).
3. D. W. Huttmacher, J. T. Schantz, C. X. F. Lam, K. C. Tan, T. C. Lim, State of the art and future directions of scaffold-based bone engineering from a biomaterials perspective. *J. Tissue Eng. Regen. Med.* **1**, 245–260 (2007).
4. M. N. Rahaman, D. E. Day, B. S. Bal, Q. Fu, S. B. Jung, L. F. Bonewald, A. P. Tomsia, Bioactive glass in tissue engineering. *Acta Biomater.* **7**, 2355–2373 (2011).
5. A. E. Jakus, A. L. Rutz, R. N. Shah, Advancing the field of 3D biomaterial printing. *Biomed. Mater.* **11**, 014102 (2016).

6. P. Ducheyne, Q. Qiu, Bioactive ceramics: The effect of surface reactivity on bone formation and bone cell function. *Biomaterials* **20**, 2287–2303 (1999).
7. R. Z. LeGeros, Properties of osteoconductive biomaterials: Calcium phosphates. *Clin. Orthop. Relat. Res.* **395**, 81–98 (2002).
8. U. Kneser, D. J. Schaefer, E. Polykandriotis, R. E. Horch, Tissue engineering of bone: The reconstructive surgeon's point of view. *J. Cell. Mol. Med.* **10**, 7–19 (2006).
9. J. Zhang, W. Liu, V. Schnitzler, F. Tancret, J.-M. Bouler, Calcium phosphate cements for bone substitution: Chemistry, handling and mechanical properties. *Acta Biomater.* **10**, 1035–1049 (2014).
10. M. Bohner, Design of ceramic-based cements and putties for bone graft substitution. *Eur. Cell. Mater.* **20**, 1–12 (2010).
11. M. Stańczyk, B. van Rietbergen, Thermal analysis of bone cement polymerisation at the cement–bone interface. *J. Biomech.* **37**, 1803–1810 (2004).
12. G. Hannink, J. J. C. Arts, Bioresorbability, porosity and mechanical strength of bone substitutes: What is optimal for bone regeneration? *Injury* **42** (suppl. 2), S22–S25 (2011).
13. W. Chen, H. Zhou, M. Tang, M. D. Weir, C. Bao, H. H. K. Xu, Gas-foaming calcium phosphate cement scaffold encapsulating human umbilical cord stem cells. *Tissue Eng. Part A* **18**, 816–827 (2012).
14. H. J. Kim, I. K. Park, J. H. Kim, C. S. Cho, M. S. Kim, Gas foaming fabrication of porous biphasic calcium phosphate for bone regeneration. *J. Tissue Eng. Regen. Med.* **9**, 63–68 (2012).
15. X. Miao, Y. Hu, J. Liu, A. P. Wong, Porous calcium phosphate ceramics prepared by coating polyurethane foams with calcium phosphate cements. *Mater. Lett.* **58**, 397–402 (2004).
16. J. J. Blaker, J. E. Gough, V. Maquet, I. Nottingher, A. R. Boccaccini, In vitro evaluation of novel bioactive composites based on Bioglass®-filled polylactide foams for bone tissue engineering scaffolds. *J. Biomed. Mater. Res. A* **67A**, 1401–1411 (2003).
17. J. A. Roether, J. E. Gough, A. R. Boccaccini, L. L. Hench, V. Maquet, R. Jerome, Novel bioresorbable and bioactive composites based on bioactive glass and polylactide foams for bone tissue engineering. *J. Mater. Sci. Mater. Med.* **13**, 1207–1214 (2002).
18. R. C. Thomson, M. J. Yaszemski, J. M. Powers, A. G. Mikos, Hydroxyapatite fiber reinforced poly(α -hydroxy ester) foams for bone regeneration. *Biomaterials* **19**, 1935–1943 (1998).
19. S. Deville, E. Saiz, A. P. Tomsia, Freeze casting of hydroxyapatite scaffolds for bone tissue engineering. *Biomaterials* **27**, 5480–5489 (2006).
20. Q. Fu, M. N. Rahaman, F. Dogan, B. S. Bal, Freeze-cast hydroxyapatite scaffolds for bone tissue engineering applications. *Biomed. Mater.* **3**, 025005 (2008).
21. F. Barrère, C. A. van Blitterswijk, K. de Groot, Bone regeneration: Molecular and cellular interactions with calcium phosphate ceramics. *Int. J. Nanomed.* **1**, 317–332 (2006).
22. K. J. L. Burg, S. Porter, J. F. Kellam, Biomaterial developments for bone tissue engineering. *Biomaterials* **21**, 2347–2359 (2000).
23. N. Travitzyk, A. Bonet, B. Dermeik, T. Fey, I. Filbert-Demut, L. Schlier, T. Schlorrdt, P. Greil, Additive manufacturing of ceramic-based materials. *Adv. Eng. Mater.* **16**, 729–754 (2014).
24. J. L. Simon, S. Michna, J. A. Lewis, E. D. Rekow, V. P. Thompson, J. E. Smay, A. Yampolsky, J. R. Parsons, J. L. Ricci, In vivo bone response to 3D periodic hydroxyapatite scaffolds assembled by direct ink writing. *J. Biomed. Mater. Res. A* **83A**, 747–758 (2007).
25. P. Miranda, E. Saiz, K. Gryn, A. P. Tomsia, Sintering and robocasting of β -tricalcium phosphate scaffolds for orthopaedic applications. *Acta Biomater.* **2**, 457–466 (2006).
26. J. Franco, P. Hunger, M. E. Launey, A. P. Tomsia, E. Saiz, Direct write assembly of calcium phosphate scaffolds using a water-based hydrogel. *Acta Biomater.* **6**, 218–228 (2010).
27. J. Cesarano III, J. G. Dellinger, M. P. Saavedra, D. D. Gill, R. D. Jamison, B. A. Grosser, J. M. Sinn-Hanlon, M. S. Goldwasser, Customization of load-bearing hydroxyapatite lattice scaffolds. *Int. J. Appl. Ceram. Technol.* **2**, 212–220 (2005).
28. A. Belcarz, A. Zima, G. Ginalska, Biphasic mode of antibacterial action of aminoglycoside antibiotics-loaded elastic hydroxyapatite–glucan composite. *Int. J. Pharm.* **454**, 285–295 (2013).
29. A. Hernandez-Soria, X. Yang, M. J. Grosso, J. Reinhart, B. F. Ricciardi, M. Bostrom, In vitro elution characteristics of antibiotic laden BoneSource™, hydroxyapatite bone cement. *J. Biomater. Sci. Polym. Ed.* **24**, 797–806 (2013).
30. J. Kim, I. S. Kim, T. H. Cho, K. B. Lee, S. J. Hwang, G. Tae, I. Noh, S. H. Lee, Y. Park, K. Sun, Bone regeneration using hyaluronic acid-based hydrogel with bone morphogenic protein-2 and human mesenchymal stem cells. *Biomaterials* **28**, 1830–1837 (2007).
31. S. Bose, S. Tarafder, Calcium phosphate ceramic systems in growth factor and drug delivery for bone tissue engineering: A review. *Acta Biomater.* **8**, 1401–1421 (2012).
32. C. H. Lee, J. L. Cook, A. Mendelson, E. K. Muioli, H. Yao, J. J. Mao, Regeneration of the articular surface of the rabbit synovial joint by cell homing: A proof of concept study. *Lancet* **376**, 440–448 (2010).
33. E. Vorndran, U. Klammert, A. Ewald, J. E. Barralet, U. Gbureck, Simultaneous immobilization of bioactives during 3D powder printing of bioceramic drug-release matrices. *Adv. Funct. Mater.* **20**, 1585–1591 (2010).
34. L. Shor, S. Güçeri, X. Wen, M. Gandhi, W. Sun, Fabrication of three-dimensional polycaprolactone/hydroxyapatite tissue scaffolds and osteoblast-scaffold interactions in vitro. *Biomaterials* **28**, 5291–5297 (2007).
35. K. H. Tan, C. K. Chua, K. F. Leong, C. M. Cheah, P. Cheang, M. S. Abu Bakar, S. W. Cha, Scaffold development using selective laser sintering of polyetheretherketone–hydroxyapatite biocomposite blends. *Biomaterials* **24**, 3115–3123 (2003).
36. S. Eosoly, D. Brabazon, S. Lohfeld, L. Looney, Selective laser sintering of hydroxyapatite/poly- ϵ -caprolactone scaffolds. *Acta Biomater.* **6**, 2511–2517 (2010).
37. A. K. Gaharwar, S. A. Dammu, J. M. Canter, C.-J. Wu, G. Schmidt, Highly extensible, tough, and elastomeric nanocomposite hydrogels from poly(ethylene glycol) and hydroxyapatite nanoparticles. *Biomacromolecules* **12**, 1641–1650 (2011).
38. B. Holmes, W. Zhu, J. Y. Li, J. D. Lee, L. G. Zhang, Development of novel three-dimensional printed scaffolds for osteochondral regeneration. *Tissue Eng. Part A* **21**, 403–415 (2015).
39. C. Heller, M. Schwentenwein, G. Russmueller, F. Varga, J. Stampfl, R. Liska, Vinyl esters: Low cytotoxicity monomers for the fabrication of biocompatible 3D scaffolds by lithography based additive manufacturing. *J. Polym. Sci. A Polym. Chem.* **47**, 6941–6954 (2009).
40. C.-H. Chen, M.-Y. Lee, V. B.-H. Shyu, Y.-C. Chen, C.-T. Chen, J.-P. Chen, Surface modification of polycaprolactone scaffolds fabricated via selective laser sintering for cartilage tissue engineering. *Mater. Sci. Eng. C* **40**, 389–397 (2014).
41. A. E. Jakus, E. B. Secor, A. L. Rutz, S. W. Jordan, M. C. Hersam, R. N. Shah, Three-dimensional printing of high-content graphene scaffolds for electronic and biomedical applications. *ACS Nano* **9**, 4636–4648 (2015).
42. A. E. Jakus, S. L. Taylor, N. R. Geisendorfer, D. C. Dunand, R. N. Shah, Metallic architectures from 3D-printed powder-based liquid inks. *Adv. Funct. Mater.* **25**, 6985–6995 (2015).
43. F. D. Beaman, L. W. Bancroft, J. J. Peterson, M. J. Kransdorf, Bone graft materials and synthetic substitutes. *Radiol. Clin. N. Am.* **44**, 451–461 (2006).
44. P. V. Giannoudis, H. Dinopoulos, E. Tsiridis, Bone substitutes: An update. *Injury* **36**, S20–S27 (2005).
45. Z. Pan, J. Ding, Poly(lactide-co-glycolide) porous scaffolds for tissue engineering and regenerative medicine. *Interface Focus* **2**, 366–377 (2012).
46. M. A. Woodruff, D. W. Huttmacher, The return of a forgotten polymer—Polycaprolactone in the 21st century. *Prog. Polym. Sci.* **35**, 1217–1256 (2010).
47. L. A. Pinczewski, A. J. Clingeleffer, D. D. Otto, S. F. Bonar, I. S. Corry, Integration of hamstring tendon graft with bone in reconstruction of the anterior cruciate ligament. *Arthroscopy* **13**, 641–643 (1997).
48. M. Nakashima, A. H. Reddi, The application of bone morphogenetic proteins to dental tissue engineering. *Nat. Biotechnol.* **21**, 1025–1032 (2003).
49. A. Yamaguchi, T. Komori, T. Suda, Regulation of osteoblast differentiation mediated by bone morphogenetic proteins, hedgehogs, and Cbfa1. *Endocr. Rev.* **21**, 393–411 (2000).
50. C. H. Lee, S. A. Rodeo, L. A. Fortier, C. Lu, C. Erskan, J. J. Mao, Protein-releasing polymeric scaffolds induce fibrochondrocytic differentiation of endogenous cells for knee meniscus regeneration in sheep. *Sci. Transl. Med.* **6**, 266ra171 (2014).
51. D. Semwogerere, E. R. Weeks, Shear-induced particle migration in binary colloidal suspensions. *Phys. Fluids* **20**, 043306 (2008).
52. W. L. Lee, C. Loei, E. Widjaja, S. C. J. Loo, Altering the drug release profiles of double-layered ternary-phase microparticles. *J. Control. Release* **151**, 229–238 (2011).
53. M.-O. Kiss, A. Levasseur, Y. Petit, P. Lavigne, Axial load-bearing capacity of an osteochondral autograft stabilized with a resorbable osteoconductive bone cement compared with a press-fit graft in a bovine model. *Am. J. Sports Med.* **40**, 1046–1052 (2012).
54. P. Zioupos, J. D. Currey, Changes in the stiffness, strength, and toughness of human cortical bone with age. *Bone* **22**, 57–66 (1998).
55. K. A. Athanasiou, C.-F. Zhu, D. R. Lanctot, C. M. Agrawal, X. Wang, Fundamentals of biomechanics in tissue engineering of bone. *Tissue Eng.* **6**, 361–381 (2000).
56. H. Shearer, M. J. Ellis, S. P. Perera, J. B. Chaudhuri, Effects of common sterilization methods on the structure and properties of poly(D,L lactide-co-glycolic acid) scaffolds. *Tissue Eng.* **12**, 2717–2727 (2006).
57. J. E. Aubin, Advances in the osteoblast lineage. *Biochem. Cell Biol.* **76**, 899–910 (1998).
58. M. Mizuno, Y. Kuboki, Osteoblast-related gene expression of bone marrow cells during the osteoblastic differentiation induced by type I collagen. *J. Biochem.* **129**, 133–138 (2001).
59. D. T. Denhardt, X. J. Guo, Osteopontin: A protein with diverse functions. *FASEB J.* **7**, 1475–1482 (1993).
60. C. M. Giachelli, S. Steitz, Osteopontin: A versatile regulator of inflammation and biomineralization. *Matrix Biol.* **19**, 615–622 (2000).
61. G. S. Stein, J. B. Lian, A. J. van Wijnen, J. L. Stein, The osteocalcin gene: A model for multiple parameters of skeletal-specific transcriptional control. *Mol. Biol. Rep.* **24**, 185–196 (1997).
62. K. Kato, H. Aoki, T. Tabata, M. Ogiso, Biocompatibility of apatite ceramics in mandibles. *Biomater. Med. Devices Artif. Organs* **7**, 291–297 (1979).
63. S. S. Lee, E. L. Hsu, M. Mendoza, J. Ghodasra, M. S. Nickoli, A. Ashtekar, M. Polavarapu, J. Babu, R. M. Riaz, J. D. Nicolas, D. Nelson, S. Z. Hashmi, S. R. Kaltz, J. S. Earhart, B. R. Merk, J. S. McKee, S. F. Bairstow, R. N. Shah, W. K. Hsu, S. I. Stupp, Gel scaffolds of BMP-2-binding peptide amphiphile nanofibers for spinal arthrodesis. *Adv. Healthc. Mater.* **4**, 131–141 (2015).
64. W. K. Hsu, M. Polavarapu, R. Riaz, G. C. Roc, S. R. Stock, Z. S. Glicksman, J. H. Ghodasra, E. L. Hsu, Nanocomposite therapy as a more efficacious and less inflammatory alternative to bone morphogenetic protein-2 in a rodent arthrodesis model. *J. Orthop. Res.* **29**, 1812–1819 (2011).
65. J. R. Dimar II, W. A. Ante, Y. P. Zhang, S. D. Glassman, The effects of nonsteroidal anti-inflammatory drugs on posterior spinal fusions in the rat. *Spine* **21**, 1870–1876 (1996).

66. I. H. Drespe, G. K. Polzhofer, A. S. Turner, J. N. Grauer, Animal models for spinal fusion. *Spine J.* **5**, S209–S216 (2005).
67. J. N. Grauer, A. R. Vaccaro, J. M. Beiner, B. K. Kwon, A. S. Hilibrand, J. S. Harrop, G. Anderson, J. Hurlbert, M. G. Fehlings, S. C. Ludwig, R. Hedlund, P. M. Arnold, C. M. Bono, D. S. Brodke, M. F. Dvorak, C. G. Fischer, J. B. Sledge, C. I. Shaffrey, D. G. Schwartz, W. R. Sears, C. Dickman, A. Sharan, T. J. Albert, G. R. Rechtine II, Similarities and differences in the treatment of spine trauma between surgical specialties and location of practice. *Spine* **29**, 685–696 (2004).
68. R. Fu, S. Selph, M. McDonagh, K. Peterson, A. Tiwari, R. Chou, M. Helfand, Effectiveness and harms of recombinant human bone morphogenetic protein-2 in spine fusion: A systematic review and meta-analysis. *Ann. Intern. Med.* **158**, 890–902 (2013).
69. N. E. Epstein, Basic science and spine literature document bone morphogenetic protein increases cancer risk. *Surg. Neurol. Int.* **5**, S552–S560 (2014).
70. E. J. Carragee, E. L. Hurwitz, B. K. Weiner, A critical review of recombinant human bone morphogenetic protein-2 trials in spinal surgery: Emerging safety concerns and lessons learned. *Spine J.* **11**, 471–491 (2011).
71. W. K. Hsu, M. Polavarapu, R. Riaz, A. C. Larson, J. J. Diegmüller, J. H. Ghodasra, E. L. Hsu, Characterizing the host response to rhBMP-2 in a rat spinal arthrodesis model. *Spine* **38**, E691–E698 (2013).

Acknowledgments: In vivo surgeries were performed with the help of E. Dielubanza. We thank N. A. Shah for preparing the tendon graft and sutured HB mesh around the tendon graft, D. Kaigler Sr. for providing the human mandible specimen pictured in Fig. 1, and N. Geisendorfer for assisting in the mechanical measurements. We thank Y.-H. Huang for establishing contacts between the group of R.N.S. and H.E.W. We are very appreciative of L. Miller and his group members C. Ethier, S. Naufel, R. Ruiz-Torres, and J. Gallego for providing the rhesus macaque and performing the calvarial surgeries. Finally, we would also like to thank C. S. Hoyuelos (the Advanced Photon Source) for support of the synchrotron microCT imaging. Use of the Advanced Photon Source supported by the U.S. Department of Energy, Office of Science, Office of Basic Energy Sciences, under contract no. DE-AC02-06CH11357. **Funding:** Biological and chemical analyses were performed in the Equipment Core Facility of the Simpson Querrey Institute for BioNanotechnology at Northwestern University. The U.S. Army Research Office, the U.S. Army Medical Research and Materiel Command, and Northwestern University provided funding to develop this facility. The Northwestern University Center for Advanced Microscopy was supported by National Cancer Institute Cancer Center Support Grant P30 CA060553 awarded to the Robert H. Lurie Comprehensive Cancer Center. The Electron Probe Instrumentation Center facility (NUANCE Center, Northwestern University) was supported by NSF grants DMR-1121262 and EEC-0118025[003]. The Northwestern University Mouse Histology and Phenotyping Laboratory and Cancer Center was supported by NCI grant CA060553. This study was also supported by the Office of Naval Research MURI Program

(N00014-11-1-0690). A.R.L. was supported by an NSF Graduate Research Fellowship. Additional funding support was provided by a gift from Google. A.E.J. was supported in part by a postdoctoral fellowship from The Hartwell Foundation as well as a National Defense Science and Engineering Fellowship. **Author contributions:** A.E.J. designed and created the HB material, 3D-printed all samples and materials used in this work, designed and conducted all experiments and characterization unless otherwise stated, and wrote the article. A.L.R. aided with experiment design and characterization and assisted with in vitro studies and characterization. S.W.J. performed all mouse biocompatibility surgeries and was responsible for mouse upkeep and care. A.K., S.M.M., and C.Y. performed the rat spinal fusion surgeries, were responsible for rat upkeep and health, and took x-rays of the implants. K.D.K. assisted with in vitro studies and mechanical characterization. S.C.Y. assisted with initial proof-of-concept 3D-printed sample fabrication and in vitro studies. C.-P.R. helped with the imaging experiments and running 3D image reconstruction software. H.E.W. histologically processed, imaged, and provided analyses for the HB calvarial samples derived from the rhesus macaque. R.D.G. provided the facilities and support for biocompatibility testing. Spinal fusion studies were designed and conducted under the guidance and within the laboratory of W.K.H. and E.L.H. W.K.H. and E.L.H. provided additional insight into the spinal fusion characterization and evaluation. S.R.S. prepared and performed laboratory microCT and synchrotron microCT on spinal fusion HB calvarial samples in addition to helping with related data analysis and interpretation. R.N.S. was the principal investigator overseeing and advising on the development and implementation of HB material and studies described within this work, as well as contributed to the preparation and editing of the manuscript. **Competing interests:** Patents pertaining to this work have been filed and are pending: (i) Room temperature synthesis and 3D printing of bioactive elastic bone for tissue engineering applications (inventors: A.E.J. and R.N.S.) and (ii) Ink compositions for three-dimensional printing and methods of forming objects using the ink compositions (inventors: A.E.J. and R.N.S.). W.K.H. has had paid consulting relationships with Bioventus, Medtronic, Bacterin, Lifenet, Mirus, and RTI. The other authors declare that they have no competing interests. **Data and materials availability:** The HB material described in this article can be obtained through a material transfer agreement with the authors and Northwestern University.

Submitted 28 March 2016

Accepted 16 August 2016

Published 28 September 2016

10.1126/scitranslmed.aaf7704

Citation: A. E. Jakus, A. L. Rutz, S. W. Jordan, A. Kannan, S. M. Mitchell, C. Yun, K. D. Koube, S. C. Yoo, H. E. Whiteley, C.-P. Richter, R. D. Galiano, W. K. Hsu, S. R. Stock, E. L. Hsu, R. N. Shah, Hyperelastic “bone”: A highly versatile, growth factor-free, osteoregenerative, scalable, and surgically friendly biomaterial. *Sci. Transl. Med.* **8**, 358ra127 (2016).



Hyperelastic "bone": A highly versatile, growth factor-free, osteoregenerative, scalable, and surgically friendly biomaterial

Adam E. Jakus, Alexandra L. Rutz, Sumanas W. Jordan, Abhishek Kannan, Sean M. Mitchell, Chawon Yun, Katie D. Koube, Sung C. Yoo, Herbert E. Whiteley, Claus-Peter Richter, Robert D. Galiano, Wellington K. Hsu, Stuart R. Stock, Erin L. Hsu and Ramille N. Shah (September 28, 2016)

Science Translational Medicine **8** (358), 358ra127. [doi: 10.1126/scitranslmed.aaf7704]

Editor's Summary

Building better bones

What if we could create custom bone implants that would trigger their own replacement with real bone? Jakus and colleagues have done just this with a promising biomaterial that can be 3D-printed into many shapes and easily deployed in the operating room. Made mainly of hydroxyapatite and either polycaprolactone or poly(lactic-*co*-glycolic acid), this "hyperelastic bone" can be 3D-printed at up to 275 cm³/hour, the authors report. It also promoted bone growth in vitro, in mice and rats, and in a case study of skull repair in a rhesus macaque. Its effectiveness, fast, easy synthesis, and ease of use in surgery set it apart from many of the materials now available for bone repair.

The following resources related to this article are available online at <http://stm.sciencemag.org>. This information is current as of October 4, 2016.

- | | |
|-------------------------------|--|
| Article Tools | Visit the online version of this article to access the personalization and article tools:
http://stm.sciencemag.org/content/8/358/358ra127 |
| Supplemental Materials | " <i>Supplementary Materials</i> "
http://stm.sciencemag.org/content/suppl/2016/09/26/8.358.358ra127.DC1 |
| Permissions | Obtain information about reproducing this article:
http://www.sciencemag.org/about/permissions.dtl |

Science Translational Medicine (print ISSN 1946-6234; online ISSN 1946-6242) is published weekly, except the last week in December, by the American Association for the Advancement of Science, 1200 New York Avenue, NW, Washington, DC 20005. Copyright 2016 by the American Association for the Advancement of Science; all rights reserved. The title *Science Translational Medicine* is a registered trademark of AAAS.